Time-Dependent Transition State Theory to Determine Dividing Surfaces and Reaction Rates in Multidimensional Systems

Master's thesis of
Robin Bardakcioglu

April 25th, 2018

First Examiner: Apl. Prof. Dr. Jörg Main
Second Examiner: Prof. Dr. Maria Daghofer

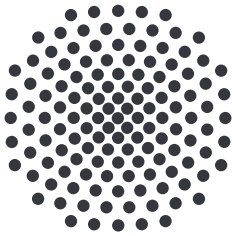

1. Institut für Theoretische Physik
Universität Stuttgart
Pfaffenwaldring 57, 70550 Stuttgart

Contents

1. Introduction

In 1889 Svante Arrhenius (*1859 - †1927) first proposed a physically justified model to describe the temperature dependence for the rate constants of chemical reactions. The Arrhenius's Law provides an empirical equation which was improved by a statistical mechanics approach in 1935 by Henry Eyring (*1901 - †1981), using what was then called an activated complex approach. Nowadays, the activated complex is known as the Transition State (TS). Transition State Theory (TST) was further developed by Hans Kramers (*1894 - †1952), where he investigated diffusion in chemical reactions with his seminal work in 1940. Forty years later, the applicability of TST was expanded by the Grote-Hynes Theory, which is based on the generalized Langevin Equation.

Nowadays, any theory that works under the assumption that there exists a Dividing Surface (DS) in phase space that divides reactants from products and is only crossed by reactive trajectories is referred to as TST [1–13]. The DS serves as tool to identify the exact time when a particle can be considered to have reacted. As such, by measuring the flux through the DS, one can determine the reaction rate of the system, as well as the rate of change for the concentration of particle species. For that measurement to be as accurate as possible, it is imperative that the DS is free of recrossings.

1.1. Introduction to Reaction Dynamics

The study of Chemical Kinetics involves itself with describing the process of chemical reactions. An important measure for these reactions is the Rate Law, since it determines the speed at which reactants are transformed into products. To better understand how the Rate Law depends on species concentration and the temperature of the system, we will provide a short introduction to the appropriate models used in chemistry.

1.1.1. Stoichiometry

To describe the transformation of reactants into products, one can use balanced stoichiometric equations. These equations describe how the ratios between reactant concentrations and product concentrations are distributed. Consider the equation

$$a\mathrm{A} + b\mathrm{B} \rightarrow c\mathrm{C} + d\mathrm{D}\,, \tag{1.1}$$

where the lowercase letters are constant integer values, while the uppercase letters are particle species. This equation expresses how a molecules of species A and b molecules

of species B are required to create c molecules of C and d of D. For instance, we can express the reaction of hydrogen and oxygen into water as

$$2\mathrm{H}_2 + \mathrm{O}_2 \rightarrow 2\mathrm{H}_2\mathrm{O}\,, \tag{1.2}$$

where two H_2 molecules and one O_2 molecule are required to form two $\mathrm{H}_2\mathrm{O}$ molecules. The stoichiometry therefore describes relationships between the concentration of species involved in a reaction.

1.1.2. Rates and Rate Laws

The Rate Law for a reaction describes the time-dependent change for the concentration [A] of any species A. By considering the stoichiometry of a reaction, we can find relationships between the concentrations of reactants and products

$$\frac{1}{a}[\mathrm{A}](t) + \frac{1}{b}[\mathrm{B}](t) = \left(\frac{1}{a}[\mathrm{A}](0) + \frac{1}{b}[\mathrm{B}](0)\right) - \frac{1}{c}[\mathrm{C}](t) - \frac{1}{d}[\mathrm{D}](t)\,. \tag{1.3}$$

A single reactant's concentration cannot change without affecting the other reactants' concentration. Therefore, if no other processes take place in the reaction, the stoichiometry also provides a relationship limited to the species of reactants and products respectively

$$\frac{1}{a}\frac{\partial[\mathrm{A}]}{\partial t} = \frac{1}{b}\frac{\partial[\mathrm{B}]}{\partial t}\,, \tag{1.4}$$

$$\frac{1}{c}\frac{\partial[\mathrm{C}]}{\partial t} = \frac{1}{d}\frac{\partial[\mathrm{D}]}{\partial t}\,. \tag{1.5}$$

By taking the time derivative of Eq. (1.3) and applying our findings for concentration changes in Eqs. (1.4) and (1.5) we can find that the rate of change for a single species describes the rates of change for any other related species

$$\frac{1}{a}\frac{\partial[\mathrm{A}]}{\partial t} = \frac{1}{b}\frac{\partial[\mathrm{B}]}{\partial t} = -\frac{1}{c}\frac{\partial[\mathrm{C}]}{\partial t} = -\frac{1}{d}\frac{\partial[\mathrm{D}]}{\partial t}\,. \tag{1.6}$$

The Rate Law is often given for the product of interest in the reaction. In general, it can be an arbitrarily complicated function of the species concentrations and other environmental factors. However, it is often expressed in simplified form as a power law

$$\frac{1}{c}\frac{\partial[\mathrm{C}]}{\partial t} = k[\mathrm{A}]^m[\mathrm{B}]^n[\mathrm{C}]^o[\mathrm{D}]^p\,, \tag{1.7}$$

where k is called the rate constant, which may depend on environmental factors such as temperature and pressure. The order of the reaction is given by the sum of the powers $r = m+n+o+p$. Note that in general, the stoichiometry of a reaction does not provide any indication for the order r of the reaction. As such, the powers $m,\ n,\ o$ and p have to be determined from measurements. This is can be achieved by analyzing how the Rate Law scales with the initial concentrations of the involved species.

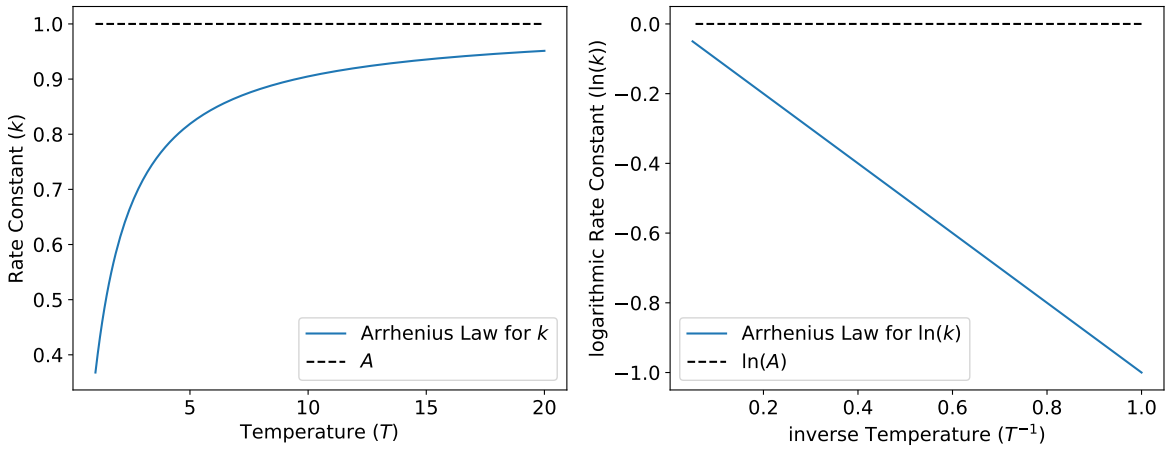

Figure 1.1.: The Arrhenius's Law for k as a function of T (left) and $\ln(k)$ as a function of $1/T$ (right). On the left, we can determine the high-temperature limit A from the asymptotic behavior of the curve. On the right, however, one can determine both A and the activation energy E_a from the $\ln(k)$-axis interception and the slope of the straight line respectively.

1.1.3. Arrhenius's Law of Rate Constants

Before Arrhenius's Law was published, it was already known that the Rate Constant k grows with the temperature T of the reaction. As a rough estimate, it was said that the Rate Constant is doubled for every 10 K. Arrhenius's Law however, provides a more accurate estimate

$$k = A \exp\left(-\frac{E_a}{k_B T}\right), \tag{1.8}$$

where k_B is Boltzmann's constant, A is the high-temperature limit of the Rate Constant and E_a the activation energy. In general, neither the high-temperature limit, nor the activation energy are known beforehand. Arrhenius's Law may also be expressed in logarithmic form

$$\ln(k) = \ln(A) - \frac{E_a}{k_B T}. \tag{1.9}$$

As a function of the inverse temperature $1/T$ the logarithmic Arrhenius's Law takes the form of a straight line. In this form, one can visually determine both the high-temperature limit A, as well as the activation energy E_a. A comparison of both expressions is shown in Fig. 1.1.

1.2. Motivation

It stands to reason that the Rate Law for the synthesis of certain substances should be controlled for optimized production. However, finding an optimal Rate Law is time consuming, since the rate constant of a reaction depends on a variety of environmental factors, such as external driving forces, temperature, dissipation, and pressure. We believe that a numerical model of chemical reactions may prove beneficial to investigate the Rate Law's dependence on such environmental parameters. As such, we investigate externally driven chemical reactions under thermal noise. We aim to find a time-dependent, recrossing-free DS in phase space, which will allow us to accurately determine when a trajectory in the molecular system transitions from a reactant configuration to a product configuration. This in turn allows us to calculate the Rate Law by using the DS to determine the time-dependent flux of reactants into products. We apply and provide methods based on TST to find the Rate Law of a classical model in the hopes to make this field of research more approachable.

1.3. Outline of this Thesis

The structure of this thesis is as follows. Chapter 2 covers the basics of the atomistic modeling used to describe chemical reactions via molecular dynamics. We describe the classical approximations used for the dynamics of an otherwise quantum mechanical system. The minimum energy path approach is also covered in these discussions, as it is a common approach in the TST for static potentials. We describe a potential to model time-dependent energy barriers of reactions, as well as the Langevin Equation, which is used to model thermal noise and other stochastic influences.

Chapter 3 covers the theoretical foundation for the TST of time-dependent systems. We discuss the use of invariant manifolds around hyperbolic fixed points and their higher-dimensional generalizations to classify reactive trajectories. Methods to reveal invariant manifolds in phase space are discussed, as well as the use of these invariant manifolds to construct recrossing-free DSs.

Chapter 4 introduces numerical methods and algorithms that are used for the investigation our system. It covers the computation of points on the normally hyperbolic invariant manifold, the use of such points to obtain a smooth approximation of the manifold, as well as the computation of reaction rates. We introduce the binary contraction method, which is a robust and exponentially fast converging algorithm to find points on normally hyperbolic invariant manifold. The algorithm is based on geometric observations of the stable and unstable invariant manifolds [14–16] in planes of the phase space and makes use of trajectory classifications. We discuss the use of artificial neural networks to approximate the DSs, introduced in chapter 3, from points computed via the binary contraction.

Chapter 5 investigates a model system under Langevin dynamics. The models and

methods introduced in the previous chapters are applied to investigate the dynamics of the system, and the influence of both friction and noise. The rate laws are computed and analyzed for different sets of parameters.

2. Atomistic Models of Chemical Reactions

2.1. Potential Energy Surfaces

To investigate the dynamics of a molecule's nuclei during a reaction, one could use a quantum mechanical approach. However, even with today's computers, such an approach is enormously time consuming, especially for large molecules. There are methods to alleviate this issue and allow us to investigate approximations of these dynamics classically. The systems discussed in this section are given by the Newtonian equations of motion

$$\dot{\mathbf{x}} = \mathbf{v}\,, \tag{2.1}$$

$$\dot{\mathbf{v}} = -\nabla V(\mathbf{x})\,, \tag{2.2}$$

where V is the potential energy, $\mathbf{x}$ the positional coordinates and $\mathbf{v}$ the corresponding velocities. For the sake of simplicity, we assume that all masses are unity.

2.1.1. Born-Oppenheimer Approximation

The Born-Oppenheimer approximation states that the dynamics of the nuclei is considerably slower than the dynamics of the electrons. This is derived from the observation, that the mass of a proton is roughly 1837 times larger than the mass of an electron. The approximation implies that, aside from external influences, the forces acting from the electron clouds onto the nuclei are purely dependent on the spatial coordination of the nuclei $\mathbf{x}$, as the configuration of the electrons can be assumed to be fully relaxed for any nuclei configuration. However, even with this approximation, we require quantum mechanical computations to determine the ground state of the electrons for any given nuclei configuration. This approximation can then be used to integrate the nuclei dynamics as if they were classical equations of motion. Integrating nuclei dynamics with energy surfaces obtained from electron ground states is referred to as Born-Oppenheimer Molecular Dynamics (BOMD).

For the purpose of applying TST to multidimensional systems, the BOMD method is still too slow. We can speed up the trajectory integration by introducing another approximation. By only calculating the ground state energy of the electrons for a small set of nuclei configurations, we can use adequate fitting and interpolation methods to

provide a classical potential $V(\mathbf{x})$. With a fully classical description of the potential, we can treat the systems that we are investigating as classical, Hamiltonian systems.

2.1.2. Minimum Energy Path and the Transition State of Static Potentials

With a classical model of a chemical reaction, we are now able to investigate the reaction path. Given prior knowledge about a molecular system, we can differentiate between reactant configurations and product configurations. With this, we can investigate whether or not trajectories of this system are reactive by determining which trajectories transition from reactants to products. This investigation alone, however, is not sufficient, as it is ignorant towards the path of the reaction and therefore ignorant towards the specific transition from reactant to product. To determine accurate reaction rates, we need to investigate at which specific time in the reaction a particle transitions from a reactant configuration into a product configuration. This Transition State (TS) is not known beforehand, but can be derived from the potential.

The Minimum Energy Path (MEP) [17] is an exceptional path in the space of the positional coordinates $\mathbf{x}$ along the time-independent potential surface $V(\mathbf{x})$. The path connects the reactant configuration with the product configuration and passes through three equilibrium points of the system, which are defined as coordinates which satisfy

$$\frac{\partial V(\mathbf{x})}{\partial x_i} = 0\,. \tag{2.3}$$

MEP-based approaches assume that reactant and product configuration are equilibrium points. It passes through a third equilibrium point along the way, which is known as the TS, but is sometimes referred to as the Activated Complex. In the MEP approach, the TS is also the lowest energy barrier that needs to be passed to reach the product configuration. This is not to say that the energy of the TS is below the energy of the reactant or product configuration. On the contrary, the TS has a higher energy than either of the two, as is illustrated in Fig. 2.1. This means in both directions along the MEP, there is a descend in the potential surface at the TS. Additionally, as it is also the lowest energy barrier in the system, there is a potential ascend in the directions orthogonal to the MEP. This means that the energy barrier that separates reactant and product configuration is, in general, a saddle point potential.

The MEP can be found through various approaches, for example through gradient descent methods. As the MEP can be found via methods that neglect the dynamics of the system, it is, in general, not a valid trajectory. This also implies that reactive trajectories may not even cross the TS directly, since they are not required to follow the MEP. It is however the path of least resistance through a reaction and can be used to investigate the transition of particles into the product region.

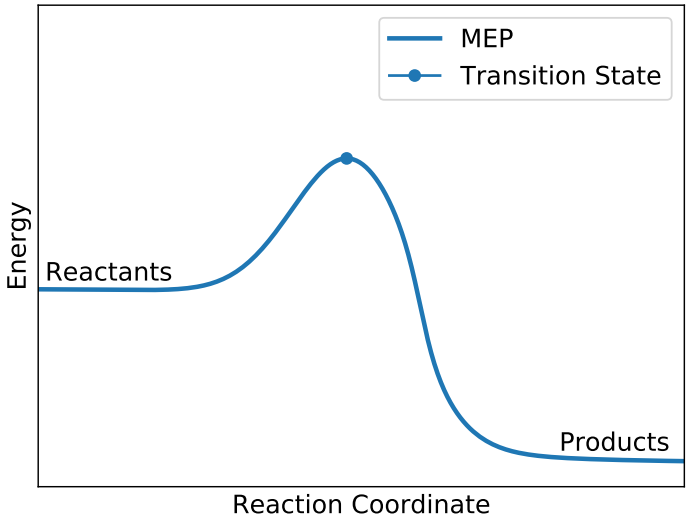

Figure 2.1.: The energy of the MEP along its parametrization for an exothermic reaction. The TS is highlighted by a dot at the energy barrier.

2.1.3. Reaction and Bath Coordinate of Static Potentials

To easily follow the transition of a molecular system from reactant configuration to product configuration, it is beneficial to express the dynamics in a coordinate system that is best suited to highlight the transition. This coordinate system should have one reaction coordinate, from which one can determine how far the reaction has progressed towards a product configuration. The corresponding velocity to the reaction coordinate has a special standing, as it is directly involved in the dynamics of the reaction coordinate. It is referred to as the reaction velocity. Any coordinate, which is coupled to the dynamics of the reaction coordinate is called a bath coordinate.

Even though the MEP neglects the dynamics of the system, its parametrization is still suited to be used as a reaction coordinate, as it not only passes through the TS, but it does so by directly connecting it to the known reactant and product configurations. One can then characterize a particle as having transitioned, if its reaction coordinate passes the reaction coordinate of the Transition State. However, the dynamics of all coordinates, including the bath coordinates, are relevant to determine the exact time of the transition and need to be included when investigating reactive trajectories.

2.2. Time-Dependent Systems

To control the reaction rate, one can apply external influences to the system. By introducing an external driving force, the potentials of the system become time-dependent. Although interesting, the dynamics of time-dependent systems are more difficult to handle. Modeling the external perturbations with time-dependent potentials may be easy, however handling the dynamics of such systems is challenging. The MEP approach is no longer sufficient to determine the TS, not only because it is now time-dependent as well, but also because the dynamics of the system is relevant for the transition. With the time-dependent motion of the energy saddle, the energy barriers of the time-independent MEPs differ for different moments in time, see Fig. 2.2. However, if one uses the moving energy barrier of the MEPs to identify the transition of a reactive particle, one would run into two inherent problems. First, due to the motion of the MEP, the reaction coordinate system would have to be time-dependent. Second, the faux transition would happen several times, as the particle has inertia, but the MEP does not. Due to these reasons, an MEP approach would not only be cumbersome, but would also lead to wrong results.

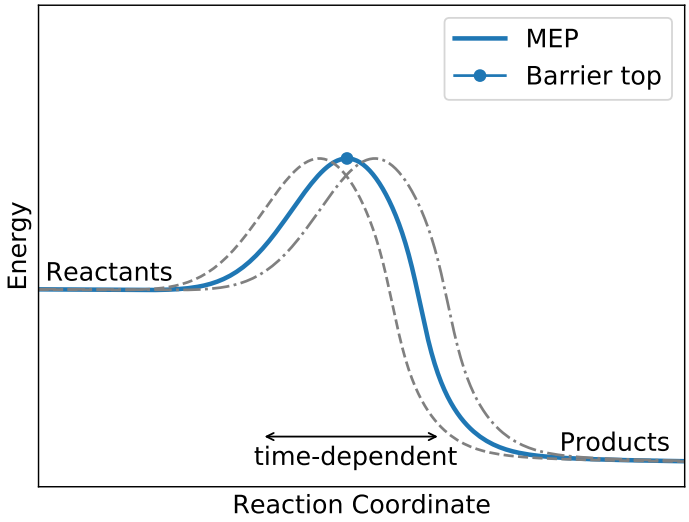

Figure 2.2.: MEPs of a time-dependent potential at different times. The motion of the energy barrier does not follow the path of a trajectory, since a particle with inertia would immediately find itself subject to a repulsive force if the saddle is moving.

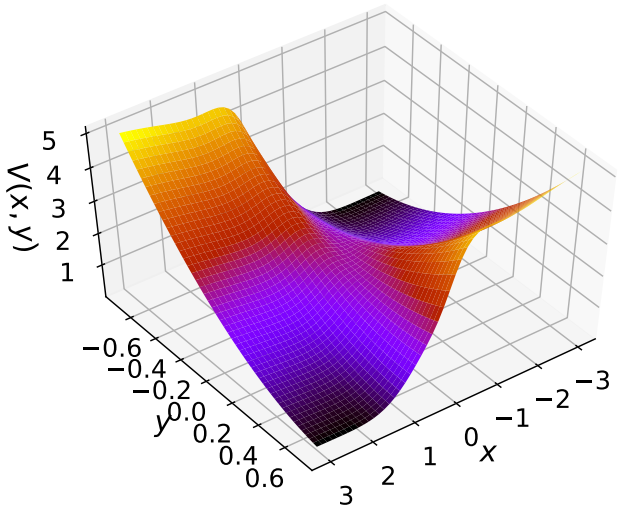

Figure 2.3.: Saddle potential given in Eq. (2.4) for parameters $E_b = 2$, $\omega_x = \pi$, $\omega_y = 2$ and $a = 1$ at $t = 0$. The color code is a visual aid for the potential, dark colors represent a small value, bright colors represent a high value.

2.2.1. Model: Driven Rank-1 Saddle Potential

As the energy barrier of the underlying potential is the bottleneck of the reaction, we expect the relevant dynamics to occur in the saddle region. To investigate the dynamics of a chemical reaction with time-dependent potentials, we model the energy barrier between reactant and product regions with a driven rank-1 saddle potential. The rank-1 saddle is a saddle point with one unstable coordinate, i.e. the potential surface descends in either direction of the coordinate, and an arbitrary number of stable coordinates. Without the MEP approach, we will use the coordinate which is strongly coupled to the instability of the saddle as the reaction coordinate, as this has been shown to be an effective coordinate to classify the transition. Specifically we investigate the two-dimensional model potential that is used in Ref. [18]

$$V(x, y, t) = E_b \exp\left(-a[x - \hat{x}\sin(\omega_x t)]^2\right) + \frac{\omega_y^2}{2}\left(y - \frac{2}{\pi}\arctan(2x)\right)^2, \tag{2.4}$$

where x is the reaction coordinate, whose dynamics is non-linearly coupled to the bath coordinate y. A snapshot of this potential is illustrated in Fig. 2.3. The saddle point for this model potential oscillates in time with the angular frequency ω_x, which ensures that the time-dependency of the potential has a noticeable impact on the dynamics in the vicinity of the saddle point. In addition to ω_x, the constants ω_y, E_b, and a are all external parameters to tune the potential.

2.3. Langevin Equation

The Langevin equation is a stochastic differential equation that describes a system under external influences whose microscopic dynamics is unknown. It is commonly used to describe a particle in a thermal environment. The dynamics of a Langevin system are often governed by a random force, together with a friction term that is coupled to the velocity of the particle.

The Langevin equation can be used to model the dynamics of Brownian motion. This motion was first discovered through the erratic movement of pollen in water. It was further investigated in Einstein's seminal paper in 1905 [19], where it was shown that there is an intrinsic relationship between friction and noise.

The Langevin equation provides equations of motion similar to Eqs. (2.1) and (2.2). However, here, the acceleration is given by

$$\ddot{\mathbf{x}} = -\gamma \mathbf{v} + \mathbf{f}(t)\,, \tag{2.5}$$

where γ is the friction coefficient, while the mass $m = 1$ and the potential $V(\mathbf{x}, t)$ are omitted. The function $\mathbf{f}(t)$ is a random force that follows

$$\langle \mathbf{f}(t) \rangle = 0\,, \tag{2.6}$$

$$\langle \mathbf{f}(t) \cdot \mathbf{f}(t') \rangle = d\xi\delta(t - t')\,, \tag{2.7}$$

where d is the number of kinetic degrees of freedom, $\delta(t - t')$ is the Dirac delta function and ξ is a constant measuring the intensity of the random force. The symbols $\langle \cdot \rangle$ denote the expectation value of the random functions.

To find the relationship between friction γ and the intensity ξ, we first solve Eq. (2.5) to find an expression for $\dot{\mathbf{x}} = \mathbf{v}$

$$\mathbf{v}(t) = \exp(-\gamma t) \left(\mathbf{v}_0 + \int_0^t \exp(\gamma t') \mathbf{f}(t')\, \mathrm{d}t' \right)\,. \tag{2.8}$$

From Eq. (2.8) we can see that for positive friction coefficients γ the contribution of the initial velocity $\mathbf{v}_0$ loses its influence on the dynamics for long times. If the friction is large, we can expect that the inertia of the particle plays a small role in the dynamics. The dynamics is instead dominated by the stochastic force. To gain an additional insight from this expression, we have to use it to compute a known value. For this, we compare it to the average kinetic energy of an ideal gas

$$\frac{1}{2} \left\langle \mathbf{v}(t)^2 \right\rangle = \frac{d}{2} k_B T\,, \tag{2.9}$$

as a model of a system subject to thermal noise, where T is the temperature of the

system and k_B is Boltzmann's constant. We evaluate this expression by computing

$$\begin{aligned}\left\langle \mathbf{v}(t)^2 \right\rangle =& \left\langle \exp\left(-2\gamma t\right) \left(\mathbf{v}_0^2 + \int_0^t \exp\left(\gamma t'\right) \mathbf{f}(t') \, \mathrm{d}t' \left(2\mathbf{v}_0 + \int_0^t \exp\left(\gamma t''\right) \mathbf{f}(t'') \, \mathrm{d}t'' \right) \right) \right\rangle \\ =& \exp\left(-2\gamma t\right) \left(\left\langle \mathbf{v}_0^2 \right\rangle + \int_0^t \int_0^t \exp\left(\gamma(t' + t'')\right) \left\langle \mathbf{f}(t') \mathbf{f}(t'') \right\rangle \, \mathrm{d}t'' \, \mathrm{d}t' \right) \\ =& \frac{d\xi}{2\gamma} + \exp\left(-2\gamma t\right) \left(\mathbf{v}_0^2 - \frac{d\xi}{2\gamma} \right) . \end{aligned} \tag{2.10}$$

By inserting this into Eq. (2.9) we find for large times and positive friction γ

$$\lim_{t\to\infty} \frac{1}{2} \left\langle \mathbf{v}(t)^2 \right\rangle = \frac{d\xi}{4\gamma} = \frac{d}{2} k_B T \, , \tag{2.11}$$

and simplifying this, we obtain

$$\frac{\xi}{2\gamma} = k_B T, \tag{2.12}$$

which is called the Einstein relation. With this, we have found a relationship between temperature T, friction γ and fluctuating forces ξ. The Einstein relation is a special case of the Fluctuation-Dissipation Theorem, which states that if an observable can be dissipated as heat, then the observable itself must fluctuate thermally. Here, the kinetic energy of a system can be transformed into heat via the friction coefficient. This in turn implies that the kinetic energy must fluctuate by virtue of a proportional, stochastic force accelerating the particle.

3. Invariant Manifolds and Dividing Surfaces

3.1. Dynamics in the Vicinity of Fixed Points

In a dynamical system, a fixed point is a set of coordinates in phase space which are not propagated further by the equations governing the dynamics. Interesting behavior is found in trajectories approaching these fixed points, as some of them are repulsed, others attracted, and others may even express a combination of both phenomena. By classifying the fixed points, we can determine the trajectory behavior in their vicinity. In this section, we will provide an overview and interpretation of the subject matter covered in Ref. [20].

3.1.1. Fixed Points

Consider the two-dimensional system

$$\dot{x} = \lambda x - xy\,, \tag{3.1}$$
$$\dot{y} = x^2 - y\,. \tag{3.2}$$

Here, λ denotes some real value. To find the fixed points of this system, we need to find coordinates which are not propagated any further, i.e. solve the governing equations for $\dot{x} = \dot{y} = 0$. We find that the coordinates $(0, 0)$ fulfill these conditions trivially, as well as $(\pm\sqrt{\lambda}, \lambda)$.

3.1.2. Linear Stability Analysis

For systems with non-vanishing linear terms, we can determine the behavior of trajectories in the vicinity of fixed points by analyzing the dynamics in a first-order approximation. Consider the fixed point $(0, 0)$ of Eqs. (3.1) and (3.2). In the vicinity of these fixed points, we find, that the dynamics is governed by the following approximations

$$\dot{x} = \lambda x\,, \tag{3.3}$$
$$\dot{y} = -y\,. \tag{3.4}$$

The solutions are $x = x_0 \exp(\lambda t)$ and $y = y_0 \exp(-t)$. From this, we can find that for any coordinate (x_0, y_0) in the close vicinity of $(0, 0)$, the y coordinate contracts towards

the fixed point. Whether or not the x coordinate contracts towards the fixed point depends on the value of λ. For $\lambda < 0$ we have contraction and for $\lambda > 0$ we have a repulsion of the x coordinate. Note that for $\lambda = 0$ we have vanishing linear terms for the dynamics in $\dot{x}$ with finite non-linear terms. Meaning, this approach does not suffice to describe the dynamics for $\lambda = 0$. When trajectories contract towards a fixed point, regardless of their incoming direction, the fixed point is described as stable. When there are contracting and repulsing directions present, the fixed point is called hyperbolic. When it is purely repulsive, it is called unstable.

3.1.3. Invariant Manifold Approach

An invariant manifold is a manifold in the phase space of a dynamical system which does not change its shape when all of its points are propagated. Trajectories, for instance, are invariant manifolds by construction, because they are a collection of points in phase space that result from a single propagated point. Due to their property, any point in phase space that propagates through an invariant manifold is part of that manifold. Because of this, trajectories cannot cross through invariant manifolds that do not fully contain them.

To investigate the dynamics in the vicinity of fixed points, it is helpful to expose invariant manifolds that contain them. To illustrate this, we solve Eqs. (3.1) and (3.2) for two cases around the fixed point $(0, 0)$. These solutions enable us to find results which are more accurate than the ones provided by the stability analysis.

First, by taking another look at Eq. (3.1) we can see that for $x = 0$ we find $\dot{x} = 0$ for any y. This means any trajectory that finds itself on the y-axis of the system cannot leave that axis. To be more formal, the collection of points

$$\mathcal{M}_s = \{(0, y) | y \in \mathbb{R}\}\,, \tag{3.5}$$

is an invariant manifold of the system. Since this manifold is a fairly simple one, it is possible to investigate the dynamics of any trajectory that it contains. In this particular case, all we need is to solve Eq. (3.2) for $x = 0$, which evaluates to

$$\dot{y} = -y\,, \tag{3.6}$$

and is equivalent to the dynamics of the linearized system. From this, we find that even with the full dynamics of the system, any point on the manifold $\mathcal{M}_s$ contracts towards the fixed point $(0, 0)$ at an exponential pace. An invariant manifold with such properties is called a stable manifold of the fixed point.

The second approach is more involved, as we cannot find a condition which is as simple to solve as the one for the stable manifold $\mathcal{M}_s$. We can, however, use an approach based on the implicit function theorem to find a local solution of y which depends on x and λ. Suppose the function $y = h(x; \lambda)$ solves the equations in the vicinity of the fixed point

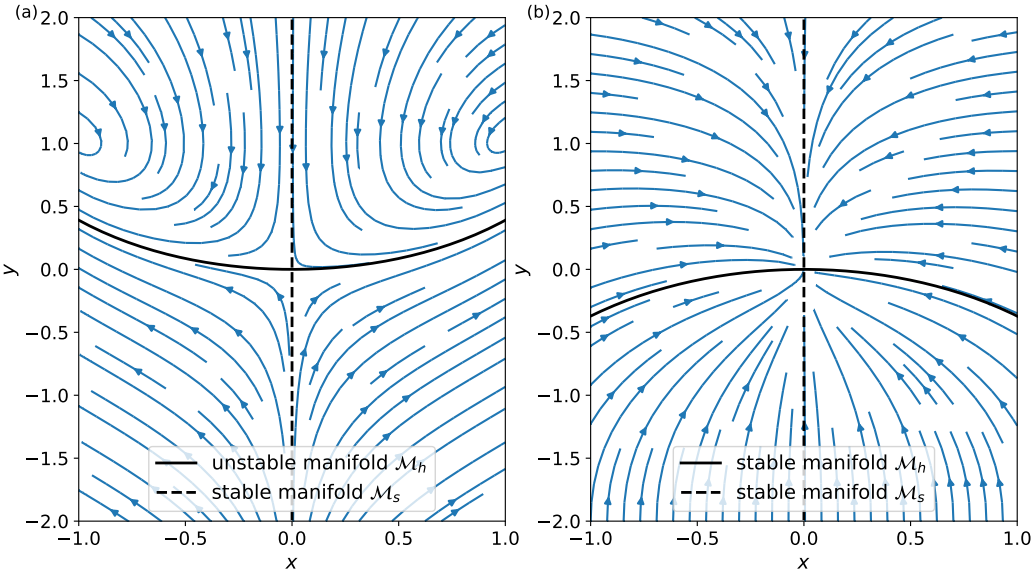

Figure 3.1.: Velocity field of Eqs. (3.1) and (3.2). (a): We see a system with $\lambda = 1$ where $\mathcal{M}_h$ is an unstable manifold and (0,0) is a hyperbolic fixed point. (b): $\lambda = -2$, where $\mathcal{M}_h$ and (0,0) are stable. We can see in both cases that the trajectories for these systems follow the path laid out for them by the invariant manifolds.

$(0, 0)$. From that, we find

$$\dot{x} = \lambda x - xh\,, \tag{3.7}$$

$$\dot{y} = -h + x^2 = \dot{x}\frac{\partial h}{\partial x}\,, \tag{3.8}$$

which yields

$$\frac{\partial h}{\partial x}x(\lambda + h) = x^2 - h\,. \tag{3.9}$$

We can use Eq. (3.9) to solve h with a power series at $x = 0$

$$h(x;\lambda) = \sum_{n=0}^{\infty} h_n(\lambda)x^n\,. \tag{3.10}$$

This yields an approximation of the function h. By enforcing the boundary condition $h_0 = 0$, the series approach yields

$$\left(\sum_{n=1}^{\infty} nh_n x^n\right)\left(\lambda - \sum_{n=0}^{\infty} h_n x^n\right) = -\sum_{n=0}^{\infty} h_n x^n + x\,, \tag{3.11}$$

by comparing the powers up until the 6th order, we find

$$h_0 = h_1 = h_3 = h_5 = 0\,, \tag{3.12}$$

$$h_2 = \frac{1}{2\lambda + 1}\,, \quad h_4 = \frac{2h_2^2}{4\lambda + 1}\,, \quad h_6 = \frac{6h_2h_4}{6\lambda + 1}\,. \tag{3.13}$$

One can continue this approach to find higher order terms. For our purposes, however, this is sufficient. By plugging in Eqs. (3.12) and (3.13) into Eq. (3.10), we find

$$h(x;\lambda) = h_2x^2 + h_4x^4 + h_6x^6 + \mathcal{O}(x^7)\,, \tag{3.14}$$

which is a symmetric polynomial of 6th order. Since the function $h(x;\lambda)$ is compliant with the dynamics of our system, the set

$$\mathcal{M}_h = \{(x, h(x;\lambda))|x \in \mathbf{R}\} \tag{3.15}$$

provides an approximation of a trajectory, which is accurate in the vicinity of the fixed point $(0, 0)$. This result differs from the result found with the linearized approach for the stability analysis, as the analysis could not predict the long-term behavior of the trajectory, which we can see in Fig. 3.1.

The dynamics on $\mathcal{M}_h$ is given by the dynamics of x confined on the graph of $y = h(x;\lambda)$. We find it by plugging Eq. (3.14) into Eq. (3.1)

$$\dot{x} = \lambda x - xh(x;\lambda)\,, \tag{3.16}$$

which still evaluates to $\dot{x} = 0$ for $x = 0$. However, we are interested in the dynamics in the vicinity of the fixed point for small values of x. By determining the slope of $\dot{x}$ at $x = 0$, we can find the sign of $\dot{x}$ at $x = \pm\varepsilon$, where ε is a sufficiently small, positive real value. We find

$$\frac{\partial \dot{x}}{\partial x}(x) = \lambda - 3h_2x^2 - 5h_4x^4 - 7h_6x^6 \tag{3.17}$$

$$\Rightarrow \frac{\partial \dot{x}}{\partial x}(0) = \lambda\,, \tag{3.18}$$

which implies for $\lambda < 0$ that

$$\dot{x}(\varepsilon) < 0\,, \quad \dot{x}(-\varepsilon) > 0\,, \tag{3.19}$$

and for $\lambda > 0$

$$\dot{x}(\varepsilon) > 0\,, \quad \dot{x}(-\varepsilon) < 0\,. \tag{3.20}$$

We can see that for $\lambda < 0$, values of x that are slightly above zero drift towards the fixed point $x = 0$. The same holds for values slightly below zero. For $\lambda > 0$ we find the inverse, any value of x in close vicinity of the fixed point drift further away from it. These results are consistent with the stability analysis, where we find stability for $\lambda < 0$ and instability for $\lambda > 0$. The difference here is, however, that the invariant manifold $\mathcal{M}_h$ gives us a more accurate picture of the dynamics in that region.

3.1.4. Classifying Reactive Trajectories using Invariant Manifolds

As TST is interested in the long-term behavior of trajectories in the vicinity of a saddle region, the dynamics around hyperbolic fixed points and Normally Hyperbolic Invariant Manifolds (see Sec. 3.3) is useful to investigate the construction of recrossing-free DSs in phase space. Hyperbolic fixed points with both stable and unstable manifolds provide us with information about the origin of a trajectory, as well as the general direction of their long-term destination. In TST this information is especially useful as it allows us to classify whether or not a trajectory is reactive based solely on where its initial conditions are in relation to the invariant manifolds.

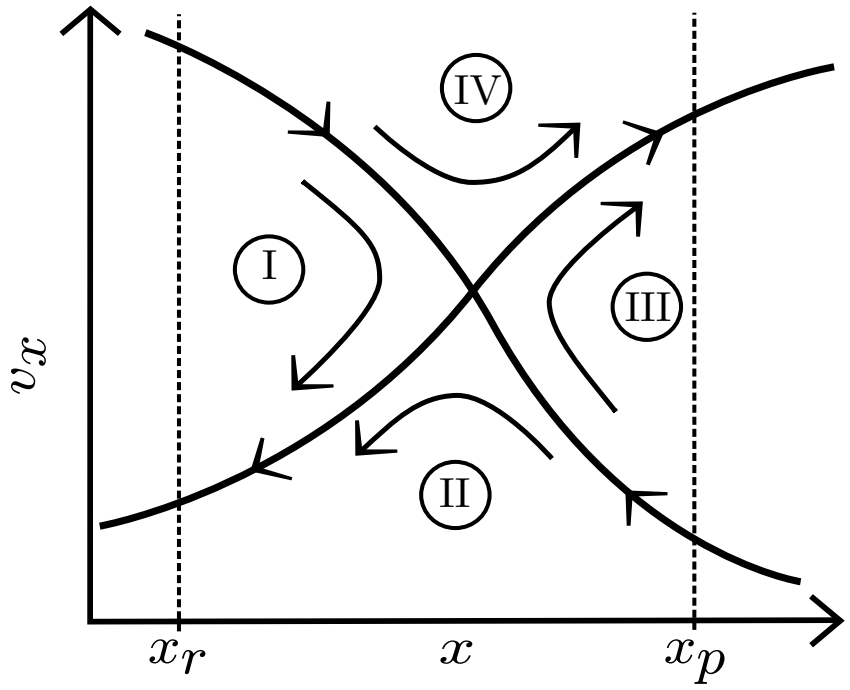

Figure 3.2.: Sketch of the phase space for a classical, one-dimensional system with reaction coordinate x and a hyperbolic fixed point, as well as known reactant and product configurations x_r and x_p. The associated stable and unstable manifolds are shown to separate the phase space into four regions, enumerated by roman numerals. The arrows indicate the heading of trajectories within these regions.

Since the stable and unstable manifold associated to a hyperbolic fixed point are invariant manifolds –which means that trajectories cannot cross them– they divide the phase space in four distinct regions. As already seen in an example system in Fig. 3.1 (a), the manifolds divide the phase space in the vicinity of the fixed point (0,0) into an upper left, upper right, lower left and lower right quadrant. The trajectories from these quadrants approach and leave the fixed point from different directions, depending on

which region contains the trajectories.

Consider a one-dimensional, reactive system with its reaction coordinate x and its corresponding reaction velocity v_x. Then the regions in phase space, that are bordered by the invariant manifolds of the hyperbolic fixed point, help us to identify reactive trajectories. This can be seen in Fig. 3.2, where these regions are referred to as region I, II, III, and IV. One can see that trajectories from region I originate from the reactant configuration x_r and return to it. Trajectories from region II originate from the product configuration x_p and are heading towards x_r. Region III is the product analogue to region I and trajectories from region IV are moving from x_r to x_p. We can conclude from this observation, that the only trajectories that play a role in determining the reaction rate are the reactive (and back-reactive) trajectories in regions II and IV, while regions I and IV would contribute to erroneous recrossings of any DS, see Sec. 3.3.2

3.2. Lagrangian Descriptors to Reveal Stable and Unstable Manifolds

Lagrangian Descriptors (LDs) [21–24] provide us with a method to reveal the stable and unstable manifolds without relying on a series expansion. By extracting a scalar value from the trajectories of a system, we can determine whether or not these trajectories are on a stable or unstable manifold of a fixed point. This is especially useful in handling multidimensional systems, as the LDs can be extracted from numerically integrated trajectories. We first discuss the LDs in a more general sense, applied to the n-dimensional system

$$\dot{\mathbf{x}} = \mathbf{f}(\mathbf{x}, t)\,, \tag{3.21}$$

afterwards we will provide a more detailed description by applying them to the system that we have investigated in Section 3.1.3.

3.2.1. Lagrangian Descriptors

Consider the function

$$\mathcal{F} : \mathbb{R}^n \to \mathbb{R}_+\,, \tag{3.22}$$

which is a positive, scalar valued function that maps the phase space of Eq. (3.21). An LD is a function

$$\mathcal{L}_\tau : \mathbb{R}^n \times \mathbb{R} \to \mathbb{R}_+\,, \tag{3.23}$$

which maps the initial conditions $\mathbf{x}_0$ and t_0 of a trajectory $\mathbf{x}$ to a positive, scalar value. The LD is the evaluation of the integral

$$\mathcal{L}_\tau(\mathbf{x}_0, t_0) = \int_{t_0-\tau}^{t_0+\tau} \mathcal{F}(\mathbf{x}(t'))\,\mathrm{d}t'\,, \tag{3.24}$$

where 2τ signifies the size of the time interval the integral covers. Depending on the choice of $\mathcal{F}$, it is useful to split the LD into forward and backward time components $\mathcal{L}_\tau = \mathcal{L}_{\tau,f} + \mathcal{L}_{\tau,b}$, given by

$$\mathcal{L}_{\tau,f}(\mathbf{x}_0, t_0) = \int_{t_0}^{t_0+\tau} \mathcal{F}(\mathbf{x}(t'))\,\mathrm{d}t'\,, \tag{3.25}$$

$$\mathcal{L}_{\tau,b}(\mathbf{x}_0, t_0) = \int_{t_0-\tau}^{t_0} \mathcal{F}(\mathbf{x}(t'))\,\mathrm{d}t'\,. \tag{3.26}$$

The significance of the LD relies wholly on the function $\mathcal{F}$ used, as this function needs to measure a property of the trajectory that describes the phase space geometries we want to investigate. A common approach is to use the norm of the velocity field,

$$\mathcal{L}_\tau(\mathbf{x}_0, t_0) = \int_{t_0-\tau}^{t_0+\tau} |\dot{\mathbf{x}}(t')|\,\mathrm{d}t'\,, \tag{3.27}$$

as this indicates the arc length of the trajectory, which in turn is an indicator to the stability of the trajectory in that region, since the longer the distance a trajectory travels for a given set of initial conditions, the more unstable are the initial conditions. For Hamiltonian systems H in particular, when we are more interested describing the positional degrees of freedom $\mathbf{q}$, we can determine their arc length with the momenta $\mathbf{p}$

$$\mathcal{L}_\tau((\mathbf{q}_0, \mathbf{p}_0), t_0) = \int_{t_0-\tau}^{t_0+\tau} \left| \frac{\partial H(\mathbf{q}(t'), \mathbf{p}(t'), t')}{\partial \mathbf{p}} \right| \mathrm{d}t'\,. \tag{3.28}$$

A special type of LD, which we will call the Time Descriptor (TD), can be applied to investigate trajectories in the vicinity of NHIMs (see Sec. 3.3). The TD tracks the amount of time a trajectory spends in the saddle region, which is confined by the reactant configuration x_r and the product configuration x_p of the reaction coordinates. For any initial condition $(\mathbf{x}_0, t_0)$ in the saddle region, we integrate the trajectories forward and backward in time and determine at which time $t_f(x_0, t_0)$ the trajectory leaves the saddle region and at which time $t = t_b(x_0, t_0)$ it enters. From this, we can compute the TD and its components

$$\mathrm{TD}(\mathbf{x}_0, t_0) = t_f(\mathbf{x}_0, t_0) - t_b(\mathbf{x}_0, t_0)\,, \tag{3.29}$$

$$\mathrm{TD_f}(\mathbf{x}_0, t_0) = t_f(\mathbf{x}_0, t_0) - t_0\,, \tag{3.30}$$

$$\mathrm{TD_b}(\mathbf{x}_0, t_0) = t_0 - t_b(\mathbf{x}_0, t_0)\,. \tag{3.31}$$

The TD is especially useful for the purposes of TST, as it is a direct measure of the time a particle lingers in the saddle region.

3.2.2. Identifying Stable and Unstable Manifolds

To identify the invariant manifolds of the previously solved system in Eqs. (3.1) and (3.2), we numerically compute the LDs in the phase space near the fixed point $(0, 0)$

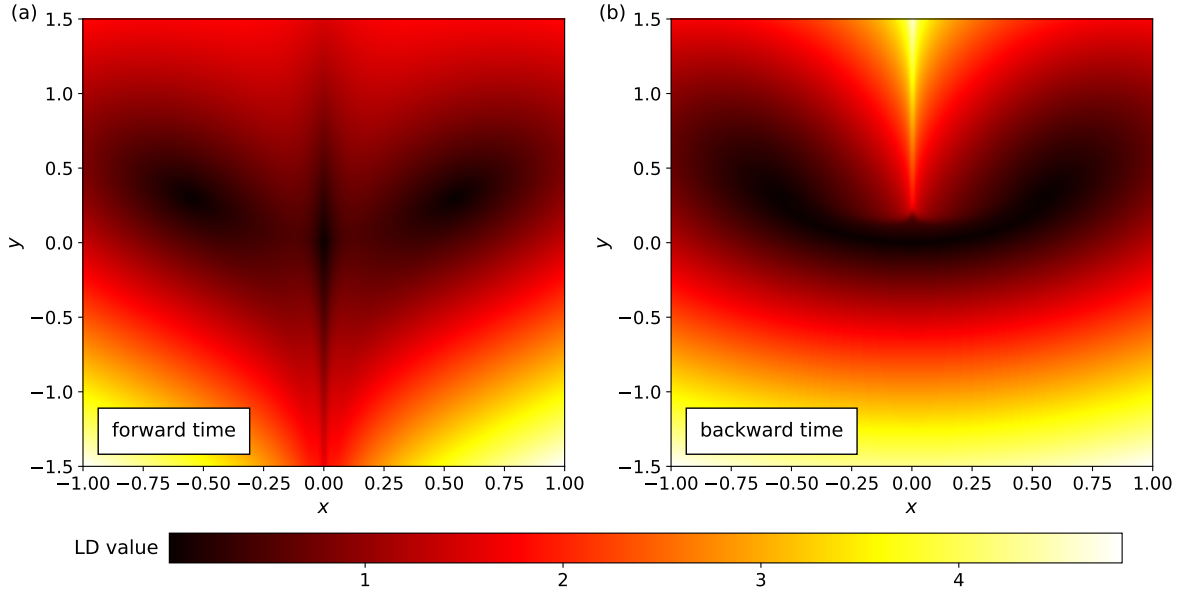

Figure 3.3.: LDs of the system given by Eqs. (3.1) and (3.2), for $\lambda = 0.3$. The minima of the forward time component (a) highlight stable manifolds, while the backwards time component (b) highlights unstable manifolds.

for $\lambda = 0.3$. The results are shown in Figs 3.3a,b. For the forward time component in Fig. 3.3a we find minima of the LD in the region of $\mathcal{M}_s$, which is consistent with the observation that $\mathcal{M}_s$ is a stable manifold. Additionally, we find minima in the vicinity of the fixed points $(\sqrt{0.3}, 0.3)$, which is to be expected, as trajectories at fixed points have no arc length. For the backward time component in Fig. 3.3, we find minima consistent with $\mathcal{M}_h$ for $\lambda = 0.3$. We can identify this manifold to be unstable, as it is a minimum of the backwards time component of the LDs and in backwards time any stable manifold in phase space is unstable in the proper time direction.

For TST, experience shows that the use of TDs to reveal the manifolds of interest is the most reliable approach [25]. As particles in the vicinity of the stable and unstable manifold linger inside the saddle region for at least one direction of integration, we can expect one of the components $\mathrm{TD_f}$ or $\mathrm{TD_b}$ to be extremal on these manifolds. Specifically, particles near the stable manifold provide a large contribution towards the forward time component, while particles near the unstable manifold do so for the backward time component. Particles close to the NHIM provide large contributions to both components, due to their vicinity to both stable and unstable manifold. Ideally, particles that are exactly on the invariant manifolds stay inside the saddle region indefinitely for at least one component of the TD. However, when using numerical integration, even trajectories that are on these manifolds may leave the saddle region in finite time, due to the errors introduced by the integration.

3.3. Normally Hyperbolic Invariant Manifolds and Dividing Surfaces

Until now, we have discussed extraordinary invariant manifolds that are attached to fixed points in phase space. Now we invert our approach and use our knowledge of stable and unstable manifolds to find another extraordinary manifold, the Normally Hyperbolic Invariant Manifold (NHIM). This manifold is given by the intersection of the closures between a stable and an unstable manifold. Since this makes the NHIM a focal point of both stable and unstable manifolds, it is an invariant manifold by itself. This allows us to interpret the NHIM as a higher-dimensional generalization of hyperbolic fixed points that is capable of containing several different trajectories at once. By using what we know about these manifolds and the trajectories in their vicinity, we can find the NHIM of a system. Knowing the NHIM, we can then use our understanding of hyperbolic fixed points and apply it to trajectories in the vicinity of the NHIM, which in turn allows us to find a recrossing-free DS.

3.3.1. Dimensionality of Normally Hyperbolic Invariant Manifolds

For a classical system, defined in Eqs. (2.1) and (2.2), with n spatial coordinates and $2n$ coordinates in phase space, we can determine the dimensionality of the NHIM. When examining a view of the reaction coordinate x and its corresponding velocity v_x in phase space, as is illustrated in Fig. 3.2, we can expect the invariant manifolds to intersect in only one point of a xv_x-plane. This observation is backed by the fact that the reaction velocity is coupled to the dynamics of the reaction coordinate.

Given a large positive value of v_x, one can expect the reaction coordinate x to grow, as the kinetic energy will eventually grow much larger than any potential energy barrier of the system. The same can be said for large negative values of v_x and the decrease of x. Given this guaranteed behavior in the limits of large velocity values, we can conclude that the general shape of the invariant manifolds in any xv_x-plane is that of a cross, if there is only one potential energy barrier present. The shape and the position of the cross, however, is generally distorted by the underlying potential and the initial conditions of the bath coordinates $(\mathbf{y}, \mathbf{v}_y)$. Since this cross exists for every set of bath coordinates, we can express the NHIM as the set

$$\mathcal{N}(t) = \{(x^{\mathrm{NHIM}}(\mathbf{y}, \mathbf{v}_y, t), v_x^{\mathrm{NHIM}}(\mathbf{y}, \mathbf{v}_y, t))|(\mathbf{y}, \mathbf{v}_y) \in \mathbb{R}^{(2n-2)}\}\,, \tag{3.32}$$

where x^{NHIM} and v_x^{NHIM} are the reaction coordinates of the NHIM for the given bath coordinates and time. As we can map the bath coordinates to a set of reaction coordinates on the NHIM, $\mathcal{N}(t)$ is $(2n-2)$-dimensional, barring its time-dependent shape.

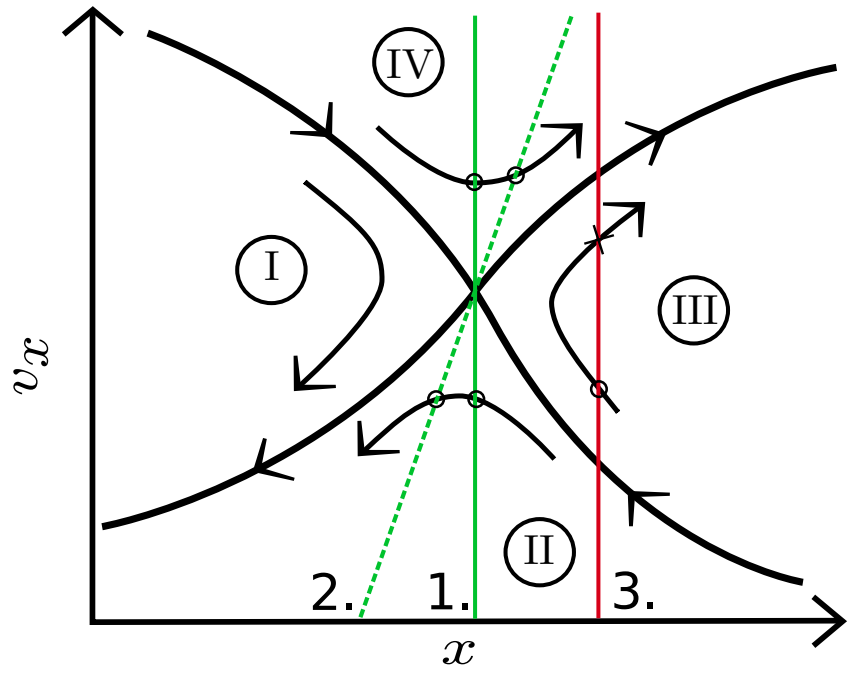

Figure 3.4.: Sketch of the stable and unstable invariant manifolds in a xv_x-plane. Lines 1., 2., and 3. show possible DSs for the system. Lines 1. and 2. pass through the NHIM and avoid regions I and III, while line 3. does not pass through the NHIM and crosses into region III. Crossings of trajectories are highlighted by small circles, while recrossings are highlighted by small crosses. We can see, that given the behavior of trajectories in regions II and IV, lines 1. and 2. serve as recrossing-free DSs. However, line 3. is recrossed by trajectories of region III.

3.3.2. Attaching a Dividing Surface to the NHIM

Since we know how to classify trajectories with the NHIM, as shown in Fig. 3.2, we can use that knowledge to attach a DS to it that is free of recrossing. Consider Fig. 3.4, it shows three lines that could be used to define a DS. These lines all have in common that they project the reaction velocity v_x onto the reaction coordinate x in a certain way. This allows us to define a DS that is $(2n-1)$-dimensional in phase space. If we were to chose a DS that passes through region III, i.e. through a region of non-reactive trajectories, as seen in Fig. 3.4 line 3., we would count erroneous crossings from particles that ultimately do not react. We can easily see in that sketch, that only if the DS is attached to the NHIM, we can minimize the number of recrossing trajectories. However, even though we attach the DS to the NHIM, there is still a freedom of choice. Since we know that the only trajectories that affect the reaction rate are the reactive and back-reactive trajectories from regions IV and II, the DS has to pass through these regions.

How the DS passes through these regions, however, is up for debate.

In general, our knowledge of the trajectories' exact heading is only accurate close to the NHIM and the stable and unstable manifolds. This means that, in theory, we do not know if the DS is truly recrossing-free for indefinitely large v_x values. It might even be the case, that a straight projection of the DS into the v_x coordinate, as shown in Fig. 3.4 for line 1., might not be recrossing-free in the close vicinity of the NHIM, when one investigates the system numerically. However, experience shows that even with the naive approach to project the v_x coordinate directly onto the NHIM, as seen in Fig. 3.4 line 1., we find a small amount of recrossings [26].

4. Numerical Methods to Determine Rate Laws

Here, we discuss the numerical methods used to compute the reaction rates. This chapter covers the computation of discrete points on the NHIM, the use of neural networks to interpolate a smooth DS from the NHIM and the computation of the rate laws by propagating an ensemble of trajectories through the DS.

4.1. Binary Contraction towards Points on the NHIM

For the sake of numerically constructing a recrossing-free DS in phase space, it is necessary to compute a large amount of points on the NHIM. This purpose necessitates the development of an efficient algorithm that is capable of computing these points accurately. One of the results of this thesis was the development of the binary contraction method [27], which fulfills these requirements. Here, we will discuss how the algorithm works and show how it can be understood from what we know about the NHIM.

4.1.1. Main Algorithm

The binary contraction method is based on the observations made in Sec. 3.1.4. In Fig. 3.2 we can see, that the four regions in phase space that classify trajectories as either non-reactive, reactive or back-reactive, can only be arbitrarily close to each other in the vicinity of the NHIM. We will use this knowledge to our advantage and provide a method that converges towards the juncture of these regions.

By integrating trajectories forward and backward in time we determine from which side particles enter and leave the saddle region. This allows us to classify the initial conditions of the trajectory to one of these regions. Using that information, we can construct a quadrangle in the xv_x-plane for a set of bath coordinates, with each vertex in one of the four regions. We then use an easy scheme to contract that quadrangle towards the juncture of the four regions, i.e. a point on the NHIM. The algorithm is as follows:

1. Construct a quadrangle with each of its vertices in one of the four regions bordered by the stable and unstable manifold.

2. Determine the midpoint between two adjacent vertices of the quadrangle.

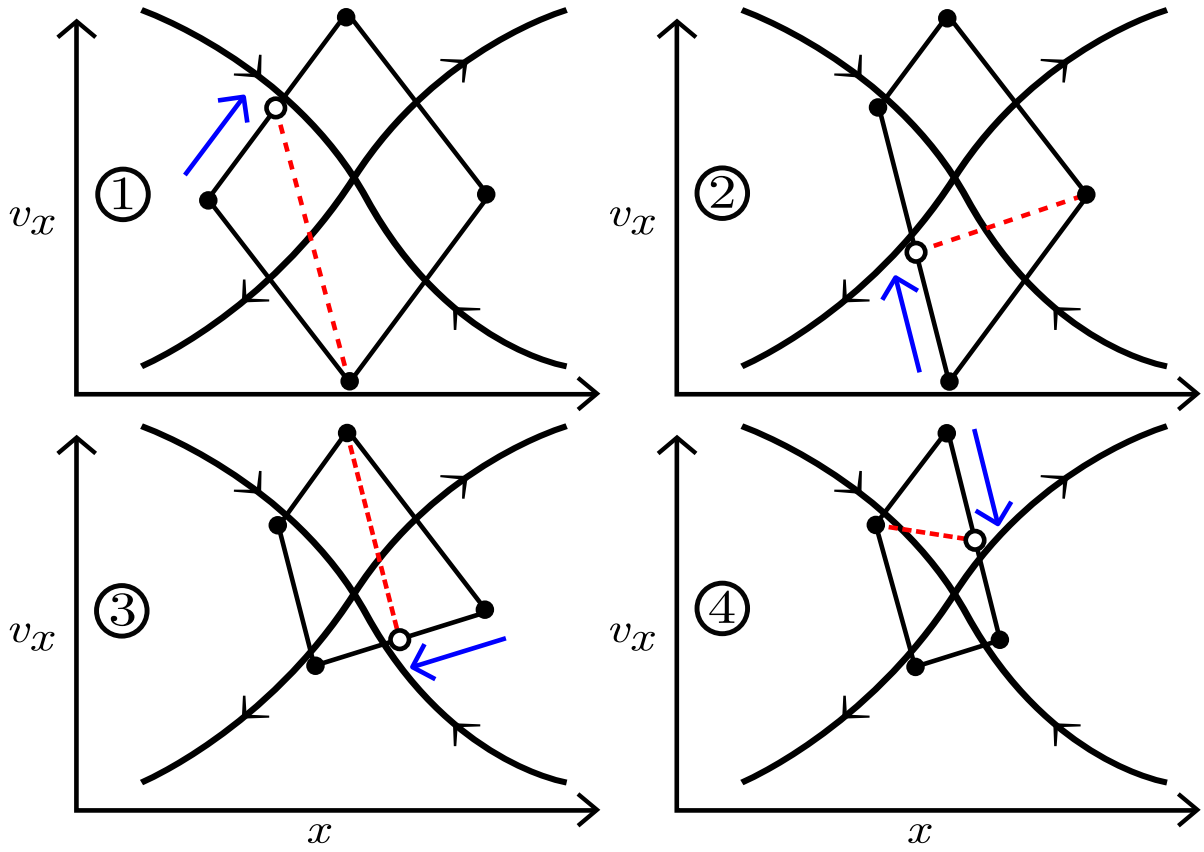

Figure 4.1.: The contraction is applied four times, once to each edge of the initial quadrangle. If the midpoint between two vertices is identified to be in the same region of either of the two, then the vertex it corresponds to is moved toward the midpoint. This contracts the quadrangle considerably towards the juncture of the regions.

3. Determine which region the midpoint corresponds to.
4. Use the new vertex to replace the vertex in the same region.
5. Repeat steps 2–4 for all edges, e.g., in a counter-clockwise manner as in Fig. 4.1, until the longest edge of the quadrangle is below a desired error tolerance.

Fig. 4.1 illustrates one pass of the algorithm along all edges of a quadrangle. Every time a vertex is moved, the length of the corresponding edge is halved. This causes the edges to contract exponentially fast with repeated application of the algorithm, which in turn causes this method to converge rapidly towards the juncture of the regions, which is part of the NHIM.

4.1.2. Efficient Initialization

For the binary contraction to work, it is important to construct a proper, initial quadrangle whose vertices are uniquely placed in one of the four regions. This could be accomplished in many ways, using approaches such as the TDs to scout for the invariant manifolds. However, methods of initialization that are computationally taxing are counter-productive, since they could overshadow the speed of the binary contraction. Therefore, initialization of the contraction needs to be handled efficiently.

The initialization of the quadrangle is handled in two steps. First, for a set of bath coordinates $(\mathbf{y}, \mathbf{v_y})$, the reaction coordinates of the NHIM are guessed. With knowledge over the structure of the invariant manifolds (see Sec. 3.3), one can then construct a quadrangle from the guess (x_0, v_{x0}). To accomplish this, apply constant shifts onto the guess for the reaction coordinates $(x_0 \pm \Delta x_0, v_{x0} \pm \Delta v_{x0})$ to construct four vertices in the xv_x-plane. These shifts are by themselves educated guesses taken from the predicted structure of the invariant manifolds and the size of the saddle region. If these four vertices are uniquely placed in the four regions, we have found a valid quadrangle from which we can start the iteration. This method works well, if the shifts are chosen to be large enough. Considering, that the algorithm converges exponentially fast, choosing a large initial quadrangle does not make a large impact on the computational time.

The guess for the reaction coordinates (x_0, v_{x0}) on the NHIM for a given set of bath coordinates can be taken from a set of already known points. One can use a lightweight extrapolation method to determine rough approximations from points of neighboring bath coordinates. By combining these extrapolation methods with additional bookkeeping that varies the shifts Δx_0 and Δv_{x_0} and keeps track of multiple vertices for each direction, one can construct a fast and robust initialization method for the quadrangle.

4.1.3. Convergence for Edge Cases

Another item to consider is the possibility of a failed contraction. A situation like this may occur when the hyperbolic point is not contained inside the quadrangle, although

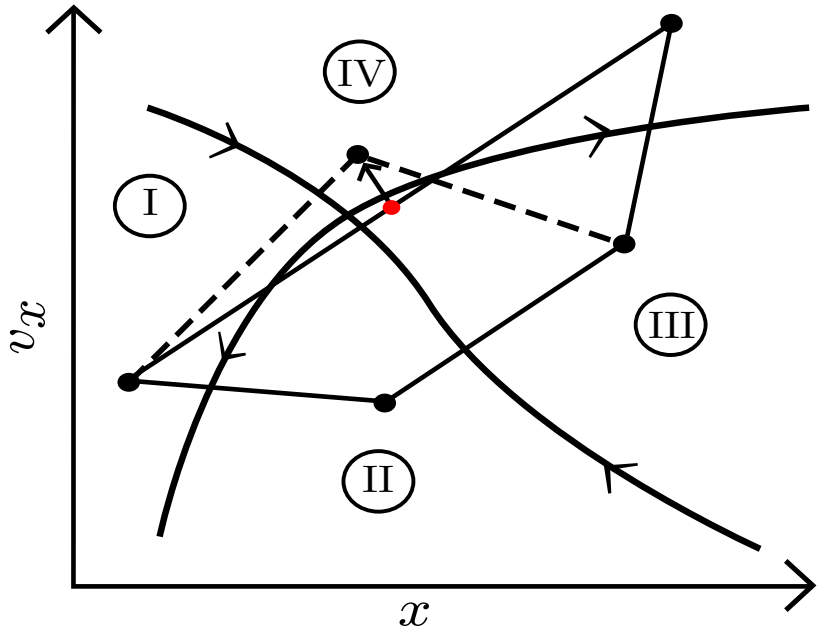

Figure 4.2.: Edge case scenario. Vertices of regions I and IV should be contracted, however their midpoint lies in region III. The failure occurs because the juncture of the four regions is not contained in the quadrangle. This problem is solved by shifting the midpoint perpendicular to the connecting line, moving it into region IV.

all vertices are still in unique regions. Fig. 4.2 shows a contraction failure when the invariant manifolds are heavily distorted. This is problematic, as the contraction method discussed is purely inclusive, meaning that it can only contract towards a quadrangle that is contained in the previous quadrangle.

The solution to this problem is also illustrated in Fig. 4.2. When a contraction failure is detected, the midpoint is shifted outwards, perpendicular to the connecting line between the vertices. This expansion has two effects. First, we increase our chances of finding a vertex inside a region that allows for contraction. Second, it allows the contraction to expand into an area that was not contained by the original quadrangle, thus allowing it to actively center itself around the juncture. As long as the perpendicular shift is chosen small enough, a net contraction can still be observed for the affected iteration step. Although this procedure requires more computational effort, we observe that, on average, the computational time required is smaller than before. This is due to the fact that by using this procedure, we avoid costly convergence failures that run until the iteration limit is reached.

4.2. Artificial Neural Networks

An artificial Neural Network (NN) is an algorithmic approach inspired by biological nervous systems. The approach mimics the way neurons in a biological system are interconnected and activated via signals passing through their synapses. Formally, a NN is a function that maps a certain set of input data supplied to via its input neurons, propagates the input through a set of neuron layers and finally yields the result with its output layer. In computing applications, NNs have been used to classify large sets of otherwise unwieldy data, as well as the interpolation of multi-variable functions whose values are cumbersome to compute. Here, we use NNs to approximate NHIMs and construct DSs [26] from training points obtained via the binary contraction.

4.2.1. Structure of a Neural Network

A feed-forward NN is a NN that only propagates its inputs forward through itself, i.e. it avoids cycling results back into previous layers. The structure of such a network is shown in Fig. 4.3, where we can see that neurons from any layer are always connected to all neurons in the following layer, except for the neuron in the output layer, as it is the last layer of the network. The value $y_j^{(n)}$ of neuron j from layer n can be expressed as

$$y_j^{(n)} = a^{(n)} \left(\sum_i w_{ij}^{(n)} y_i^{(n-1)} + b_j^{(n)} \right) , \tag{4.1}$$

where $w_{ij}^{(n)}$ are called the weights of the layer, which determine how the outputs of the neurons from the previous layer are weighted for the activation of the current neuron, $b_j^{(n)}$ is the bias value for the current neuron and $a^{(n)}(\,\cdot\,)$ is the activation function of the current layer. Of course, for the input layer $n = 0$ the values of the neurons are given by the input data $\mathbf{x}$ of the NN. This makes the NN a function composition of N layers to produce the output

$$\mathbf{y}(\mathbf{x}) = (\mathbf{y}^{(N)} \circ \mathbf{y}^{(N-1)} \circ ... \circ \mathbf{y}^{(1)})(\mathbf{x}) \,. \tag{4.2}$$

We can see, that the activation function of the layers play a crucial role for the function of the NN. In general, it is necessary to use non-linear activation functions, otherwise the NN could be simplified to a linear map of the input data. If a differentiable NN is desired, one can choose differentiable activation functions to guarantee that property.

4.2.2. Training a Neural Network

Finding the right weights and biases for Eqs. (4.1) and (4.2) to fulfill the purpose of the NNs, is an involved process. To accomplish this, one typically uses an optimization

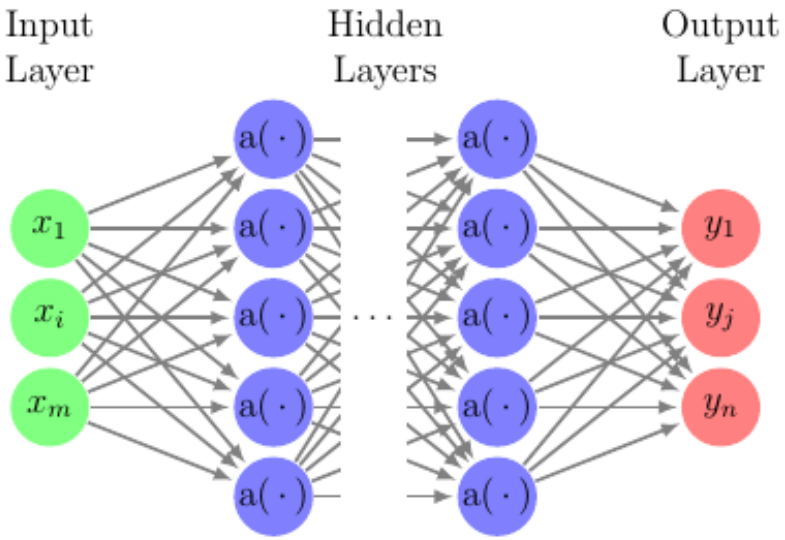

Figure 4.3.: Taken from [28]. The structure of a feed-forward NN with m input neurons and n output neurons and arbitrary hidden layers with activation function $a(\,\cdot\,)$.

process that minimizes the NNs deviation for a given set of training data. The deviation from the data is given by a scalar cost function

$$C(\mathbf{x}_0, \mathbf{y}_0) = \frac{1}{2}\|\mathbf{y}(\mathbf{x_0}) - \mathbf{y}_0\|^2\,, \tag{4.3}$$

where $\mathbf{y}_0$ is the training value for input $\mathbf{x}_0$. The exact definition of the cost function may vary, but as long as it is positive definite, differentiable and zero if $\mathbf{y}(\mathbf{x}_0) = \mathbf{y}_0$, it can be used for optimization based on gradient descent methods.

Typically, a stochastic gradient descent method is used to optimize the weights and biases of a NN. For every step in the training process, the weights and biases are shifted via the gradients of the cost function

$$\hat{w}_{ij}^{(n)} = w_{ij}^{(n)} - \eta\frac{\partial C}{\partial w_{ij}^{(n)}}\,, \tag{4.4}$$

$$\hat{b}_{j}^{(n)} = b_{j}^{(n)} - \eta\frac{\partial C}{\partial b_{j}^{(n)}}\,, \tag{4.5}$$

where η is the learning rate, i.e. the rate at which the gradient of the cost function affects the new weights $\hat{w}_{ij}^{(n)}$ and biases $\hat{b}_{j}^{(n)}$. Evaluating the gradients for every component of the cost function is computationally expensive for large NNs. Therefore, to alleviate the computational cost, the stochastic gradient descent method only evaluates random components of the gradients for every training iteration. Even though this approach only approximates a gradient descent method, the stochastic gradient descent method has been shown to converge towards local minima, and in some cases even global minima.

4.2.3. Using Neural Networks to Approximate NHIMs

Given a discrete subset $\tilde{\mathcal{N}}(t)$ of the NHIM $\mathcal{N}(t)$, defined in Eq. (3.32), for discrete intervals of t, we can optimize the weights and biases of a NN to approximate the complete set $\mathcal{N}(t)$, for any time t. In theory, we can approximate every differentiable NHIM with a NN, however in practice, the accuracy of the approximation relies heavily on the layer geometry, the type, and activation functions of the NN, as well as the optimization algorithm used, not to mention the shape of the training data. If, for instance, the NHIM $\mathcal{N}(t)$ contains erratically moving structures, then it is necessary to both provide training data with sufficient resolution in these areas and use a layer geometry with sufficient complexity to approximate these structures.

For TST, we use NN approximations of the NHIM to construct DSs for rate calculations. This is done in order so save unnecessary computational effort in calculating the NHIM at an extremely high resolution. In practice, the NNs are trained to compute points on the NHIM as functions of the bath coordinates and time. This means that for a system with n spatial coordinates, the NN would require $(2n-1)$ input neurons, $(2n-2)$ for the bath coordinates and 1 for the time t. Depending on the choice of the DS, the requirements for the output neurons differ. For instance, if one were to choose line 2. in Fig. 3.4 as a DS, one would need both the reaction coordinate and its corresponding velocity on the NHIM to construct the DS. However, if one were to choose line 1. in the same figure, then the only output that is required of the NN is the reaction coordinate x.

For the time-dependent potential shown in Fig. 2.3 and Eq. (2.4), experience shows that a NN with only one output neuron for the reaction coordinate x converges much faster than a NN with two outputs. Specifically, a NN with 3 input neurons, followed by a hidden layer with 40 and 10 neurons, as well as one output neuron, shows promising results [28]. All layers, except for the last layer, use the inverse tangent as activation function

$$a(x) = \arctan(x)\,, \tag{4.6}$$

while the last layer produces a linear combination of the previous neurons' values.

4.3. Computing Reaction Rates

With a NN that can approximate the reaction coordinate of the NHIM for any given bath coordinate and time, we can now compute reaction rates.

4.3.1. Tracking Particle Distance from DS

By tracking the distance of a particle to the DS, i.e. the difference between the reaction coordinate of the particle and the NHIM, we can determine on which side of the DS the particle is located. This allows us to determine whether or not the particle is a reactant

or product for every time step of the integration. Furthermore, given an ensemble of particles, this allows us to track the number of reactants $N_r(t)$.

Not only is the distance of the particle relevant, but also the number of times the particle crosses the DS. This can be observed in the number of times the distance changes its sign. Ideally, we only want the particle to cross the DS once, as recrossings of the DS would result in the overestimation of the reaction rate. However, since the usage of a NN based approach is a compromise between performance and accuracy, we may expect some amount of recrossing caused by errors in approximating the NHIM.

4.3.2. Obtaining Rate Laws and Constants for Unimolecular Reactions

When investigating a unimolecular reaction, knowing $N_r(t)$ is enough to characterize the rate law of the reaction, since the number of products takes the form

$$N_p(t) = N_r(0) - N_r(t)\,. \tag{4.7}$$

For the rate law, this means that

$$\frac{\partial N_p}{\partial t}(t) = -\frac{\partial N_r}{\partial t}(t)\,. \tag{4.8}$$

Given what we know about rate laws (see Eq. (1.7)), we expect to find a single rate constant for the reaction. For a first order reaction, the rate law would take the form

$$\frac{\partial N_p}{\partial t}(t) = kN_r(t)\,, \tag{4.9}$$

with Eq. (4.8) this would mean that N_r is an exponential function of the form

$$N_r(t) - N_r(\infty) = N_{r,0}\exp\left(-kt\right), \tag{4.10}$$

where $N_r(\infty)$ is the integration constant, signifying the number of reactants that have not reacted and $N_{r,0}$ is the number of initial reactants that are going to react. A positive rate constant k implies that the number of reactants in the system would decay exponentially.

One thing to consider when investigating the rate law is the settling time of the reaction. The rate law at the start of the reaction may not reflect the rate law for the majority of the time. This settling time at the beginning may be a consequence of the initial ensemble of particles propagated for the reaction. Due to this, it may be useful to investigate how $N_r(t)$ behaves at different times of the reaction. When expecting a first order reaction, for instance, investigating $N_r(t)$ on a logarithmic scale will reveal regimes of exponential decay as straight lines. By identifying such regimes, one can determine the rate constant of the first order reaction by fitting Eq. (4.10) to the measurements.

5. Investigating a Model System under Langevin Dynamics

We investigate the invariant manifolds of a model system under Langevin Dynamics, compute points on the NHIM, determine a DS, and calculate the rate law. By investigating the effects of friction and temperature on trajectories of the system as well as the NHIM we will try to understand the difficulties that we might encounter. By approximating the NHIM, we construct a smooth DS to extract the rate constant for the system under different friction and temperature parameters.

5.1. Preliminary Investigation without Langevin Dynamics

To acquire a preliminary understanding of the results that we should expect, we first investigate the model system without Langevin Dynamics, i.e. without friction and noise. We choose a parameter set where Eq. (2.4) takes the form

$$V(x, y, t) = 2 \exp\left(-[x - 0.4 \sin(\pi t)]^2\right) + 2\left(y - \frac{2}{\pi} \arctan(2x)\right)^2, \tag{5.1}$$

in simulation units. With these parameters, the saddle oscillates with a period of $T = 2$. For this potential, we investigate the saddle region $x \in [-1.5, 1.5]$.

5.1.1. Time Descriptors of the Saddle Region

To reveal the stable and unstable invariant manifolds for a certain set of bath coordinates (y, v_y), we compute the TDs (see Sec. 3.2) in the plane of the reaction coordinate and its velocity (x, v_x) within the saddle region. Figs. 5.1 (a) and (b) show the backward and forward time component of the TDs, respectively. This allows us to identify that the line of maxima depicted in Fig. 5.1 (a) is the unstable manifold and Fig. 5.1 (b) depicts the stable manifold. Knowing which of the manifolds are stable and unstable allows us to identify the heading of trajectories close to these manifolds.

Fig. 5.2 (a) shows the complete TD of the saddle region for $y = v_y = 0$ and $t = 0$. We can clearly see the shape of a cross, which splits the plane in four distinct regions. Together with the results depicted in Figs. 5.1 (a) and (b), we can determine

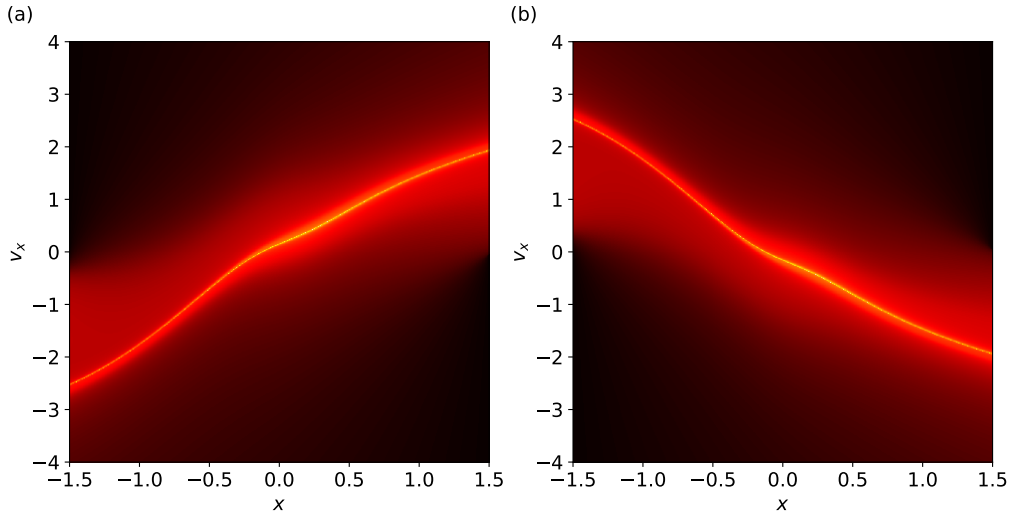

Figure 5.1.: TD components for bath coordinates $y = v_y = 0$ and time $t = 0$. Dark colors signify small values, bright colors large values. The backwards time component (a) reveals the unstable manifold and forward time component (b) reveals the stable manifold.

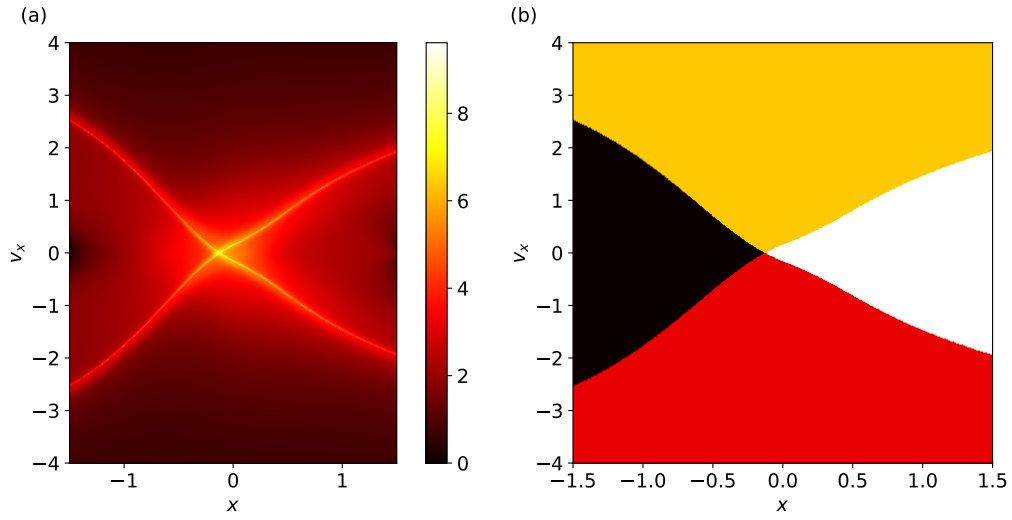

Figure 5.2.: (a): Complete TD from the components of Figs. 5.1 (a) and (b). Their intersection highlights the point on the NHIM for bath coordinates $y = v_y = 0$ at time $t = 0$. (b): Region mapping of the same plane in phase space, highlighting different types of trajectories. The mapping was calculated independent from the TD method, to verify the results.

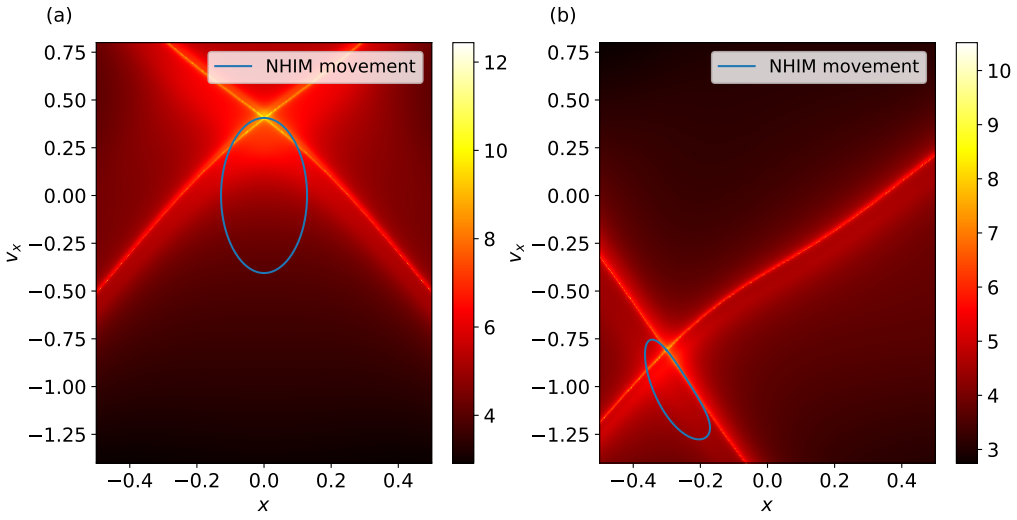

Figure 5.3.: Time-dependent motion of the NHIM in the (x, v_x) plane for $t \in [0, T]$. A mapping of the TDs at time $t = 0$ is shown in the backgrounds. The movement of the NHIM forms a closed loop with the oscillation of the saddle. Results in (a) were computed for bath coordinates $y = v_y = 0$, results in (b) were computed for bath coordinates $y = 0.5,\ v_y = 2$. The extents of the coordinate axes are intentionally chosen to be the same for both plots.

the classifications of the trajectories from the TDs, as depicted in the sketch Fig. 3.2. We find, that the trajectories from the upper region are reactive, the trajectories from the lower region are back-reactive, and the trajectories in the left and right regions do not react at all. The classifications have been verified in the direct calculation of the trajectories depicted in Fig. 5.2 (b). We can see the four different regions in phase space, whose trajectories have been classified independently of the invariant manifolds. Trajectories were integrated forward and backward in time for every coordinate in the highlighted region and were classified according to which direction they entered and left the saddle region. As we can see, the shapes of the regions depicted in Fig. 5.2 (b) match the regions bordered by the maxima of the TDs in Fig. 5.2 (a). The trajectory headings determined from the invariant manifold approach match the results from the direct computation as well.

5.1.2. Time-Dependent Motion of the NHIM

By revealing the invariant manifolds for a few bath coordinates, we now know where to expect reactive and back-reactive trajectories. With this knowledge we can safely construct good initial conditions for the Binary Contraction (see Sec. 4.1.1), even for bath coordinates that have not been explored with the TDs. Here, we use the Binary

Contraction to compute the NHIM for several times $t \in [0, T]$ over the oscillation period of the potential.

The time-dependent motion of the NHIM is shown in Figs. 5.3 (a) and (b), for two different bath coordinates. In both figures we can see that the NHIM forms a closed loop in the xv_x-plane for the corresponding bath coordinates. This is to be expected, as the underlying potential for the system is periodic. In Fig. 5.3 (a) we can see a symmetric path of the NHIM around the origin of the xv_x-plane. In Fig. 5.3 (b) we can see that this is not the general case, as the path of the NHIM does not circle the origin, nor does it possess an obvious symmetry. Keep in mind that even though the NHIM itself is an invariant manifold, the paths shown in Figs. 5.3 (a) and (b) are, in general, not trajectories of the system. They are just a view of the NHIM for a fixed set of bath coordinates.

5.1.3. Interpolating the NHIM

Using the Binary Contraction, we computed a total of roughly $10,000$ points on the NHIM, for bath coordinates in the interval $y \in [-4, 4]$, $v_y \in [-8, 8]$ and time coordinates in the interval $t \in [-0.5, 2.5]$. These points were used to train a NN with three input neurons, followed by a hidden layer of 60 neurons and one with 20 neurons. The net had only one output neuron and was trained to approximate the reaction coordinate x. The training iterated over the training data roughly $10,000$ times, which is a very short training time for NNs. Regardless, this amount of training was already enough to provide the necessary accuracy to minimize the recrossings during rate calculations.

As the NHIM for any given bath coordinate moves in a smooth, closed loop, the time-dependent motion of the NHIM was not hard to approximate by the NN. This is the reason why a fairly small set of training data was enough to train a small NN to approximate the NHIM. The NHIM at $t = 0$, computed with the Binary Contraction, can be seen in Fig. 5.4. The color coding shows the local deviation of the NN approximation from the real data. We find that the errors are largest in areas where the NHIM is strongly warped. This is to be expected, given that the training data provided the same resolution of points for the highly warped regions near the origin and the less warped regions. This means that areas which are harder to interpolate were weighted as much in the training as areas that are easier to interpolate.

5.2. The Effects of Langevin Dynamics on the NHIM

In this section we investigate how friction γ and temperature $k_B T$, introduced in Eqs. (2.5) and (2.9), affect the dynamics of our model system and the time-dependent motion of the NHIM. To this end, we investigate the invariant manifolds using the same approaches that we have used in the previous section 5.1 to investigate our model system without Langevin dynamics.

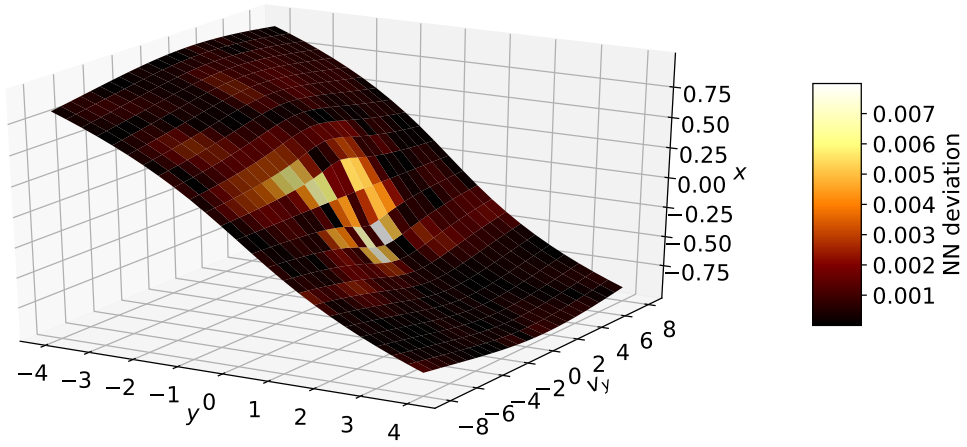

Figure 5.4.: NHIM for the noise- and frictionless model system given in Eq. (5.1) for $t = 0$. The reaction coordinate x is shown as a function of the bath coordinates y and v_y. The reaction velocity v_x has been omitted for visualization purposes. The face colors of the surface represent the deviation of the NN approximation from points computed via Binary Contraction.

5.2.1. Effects of Friction on Time Descriptors

Fig. 5.5 shows the TDs in the xv_x-plane for the bath coordinates at $y = v_y = 0$ and time $t = 0$, for the model system under Langevin dynamics. In this particular case, we are investigating the TDs at a temperature of $k_BT = 0$ with friction coefficients $\gamma \in \{0, 0.3, 0.8, 2.0\}$. Fig. 5.5 (a) shows a reference system without Langevin dynamics, while Figs. 5.5 (b), (c), and (d) show how different values of friction influence the invariant manifolds.

By looking at the scale to the right of these each figures, we can see that the TD values of the stable manifolds increase with friction. This can be explained with the influence of the friction on the forward and backward time components of the TDs. In forward time, the friction reduces the initial velocities of the trajectories, as well as the influence of the particle's inertia towards the dynamics. This causes the particle to stay inside the saddle region for a much longer than usual. This is especially true for trajectories near the stable manifold. In backwards time, the effects of friction are reversed. Instead of dampening the initial velocities, we find that the friction causes the velocities to increase exponentially (see Eq. (2.8) for reference). This causes trajectories in backwards time to escape the saddle region much faster, which in turn implies that the backward time component of the TDs is smaller than usual.

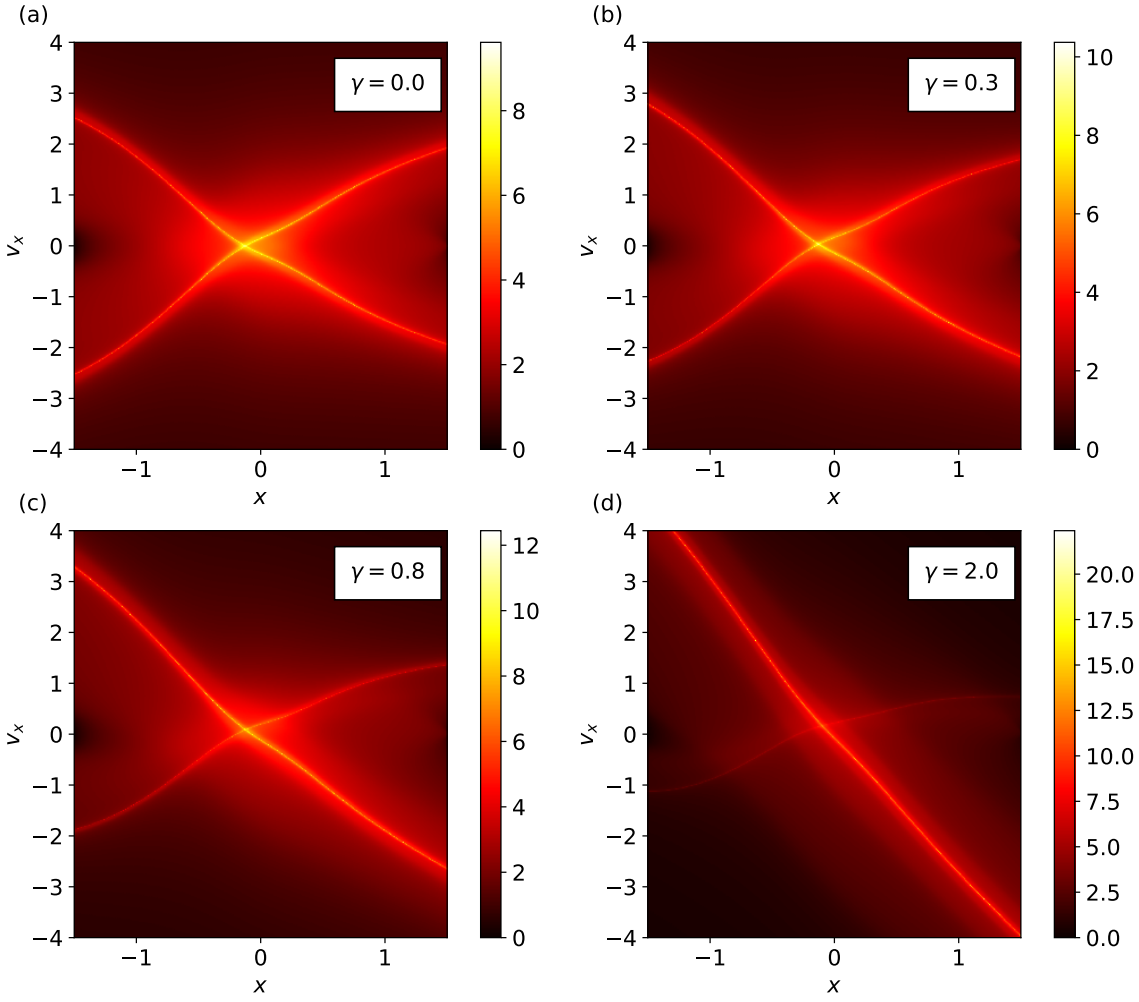

Figure 5.5.: TDs of the xv_x-plane for bath coordinate $y = v_y = 0$ and time $t = 0$, for increasing friction coefficients. We can clearly see crosses for all friction values, indicating the stable and unstable manifolds.

We also observe, that the invariant manifolds shift with increasing friction. For a small friction value, as depicted in Fig. 5.5 (b), the invariant manifolds do not change much. However, for medium frictions, as shown in Fig. 5.5 (c), we see that the stable manifold is straightened out for larger $|x|$ and its slope becomes steeper, while the slope of the unstable manifold decreases. This occurrence can also be observed for a high friction coefficient, illustrated in Fig. 5.5 (d). However, even though the invariant manifolds shift noticeably, their intersection is only shifted slightly.

5.2.2. TDs and Erratic Motion of NHIMs under Noise

For non-zero temperatures, the dynamics of the system changes considerably. Not only do the coordinates of the NHIM change, their time-dependent motion is also highly erratic under certain circumstances. This is illustrated in Fig. 5.6, where we see the time-dependent motion of the NHIM over the period of the underlying potential, for four different sets of temperature and friction. For these particular calculations, the same sequence of fluctuating forces was used, aside from their intensity ξ, which depends on temperature and friction (see Eq. (2.12)).

For low temperatures and friction, as seen in Fig. 5.6 (a), we find that the NHIM's movement still roughly resembles a closed loop. Note that the time-dependent motion of the NHIM is not periodic, since the fluctuating force is not periodic. The influences of stochastic forces are clearly visible, as we can see the fluctuation in the path of the NHIM. By increasing the friction, as seen in Fig. 5.6 (b), we find that the small fluctuation has a much higher impact on the path of the NHIM. This can be explained due to the fact that a high friction coefficient reduces the contribution of a particles inertia to the dynamics. Therefore, the path that trajectories take through the system are much more influenced by the acting force. This, of course, also affects the NHIM, as the fluctuating force in the vicinity of the potential saddle can decide whether or not a particle is reactive. The same can be seen in Fig. 5.6 (c), where we observe the NHIM for high temperatures and low friction. In this case, the high intensity of the fluctuating force causes the NHIM to move erratically, similar to the previous case with low temperature and high friction. Unsurprisingly, for high temperature and friction we find an extremely erratic NHIM, as can be seen in Fig. 5.6 (d).

In the case of high friction and high temperature, the TDs may indicate that there might be more than one stable and unstable manifold. This can be seen in Figs. 5.6 (b), (c), and (d), where one can see sharp gradients in the TDs other than the most prominent ones. This is especially true for Fig. 5.6 (d), as one can easily discern a second cross next to the NHIM. These additional crosses and their edges should not be mistaken for invariant manifolds, as their edges are not local maxima of the TD. Rather, they are edges of plateaus in the TD values. This is further illustrated in Figs. 5.7 (a) and (b). These figures show both the TD values for high temperature and friction, as well as the trajectory regions, classifying trajectories as either non-reactive, reactive or back-reactive. We can clearly see that only the local maxima of the TDs indicate the

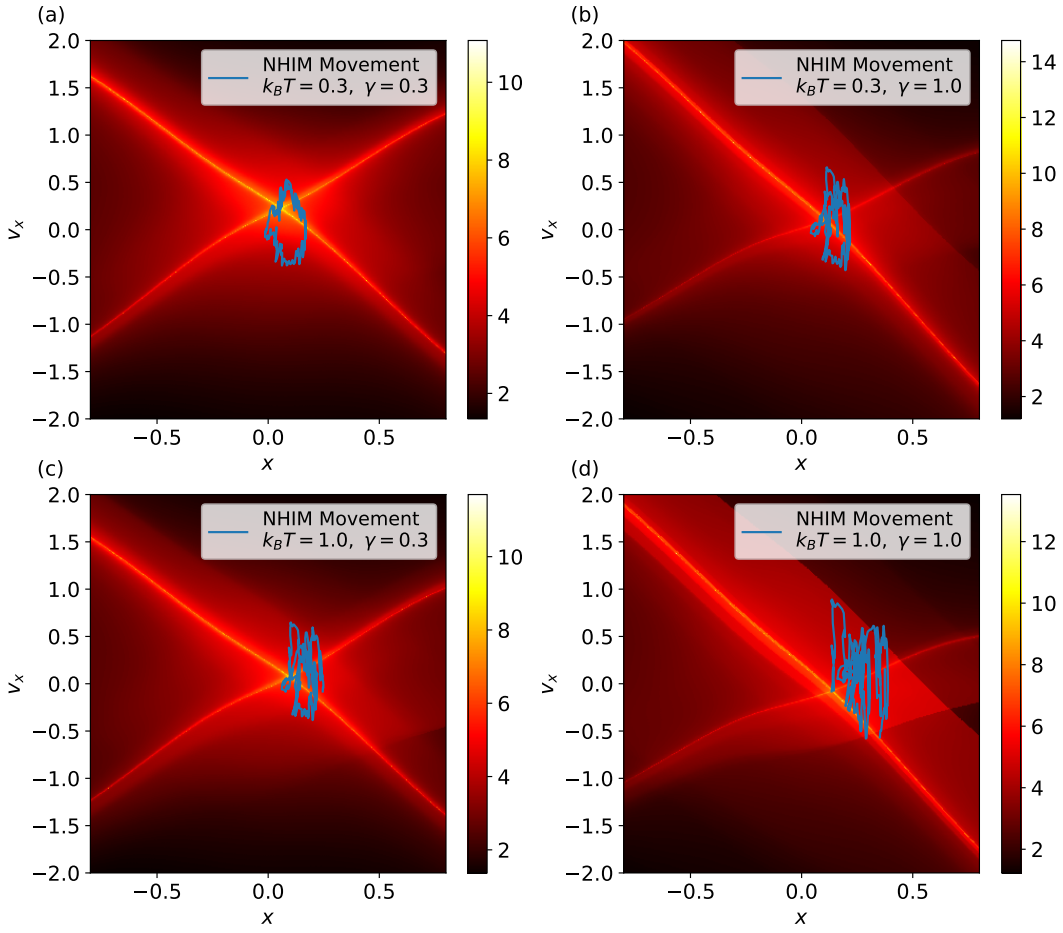

Figure 5.6.: TDs of the xv_x-plane for bath coordinates $y = v_y = 0$ and $t = 0$, for different combinations of temperature and friction. The plotted line indicates the time-dependent motion of the NHIM over the period of the saddle potential.

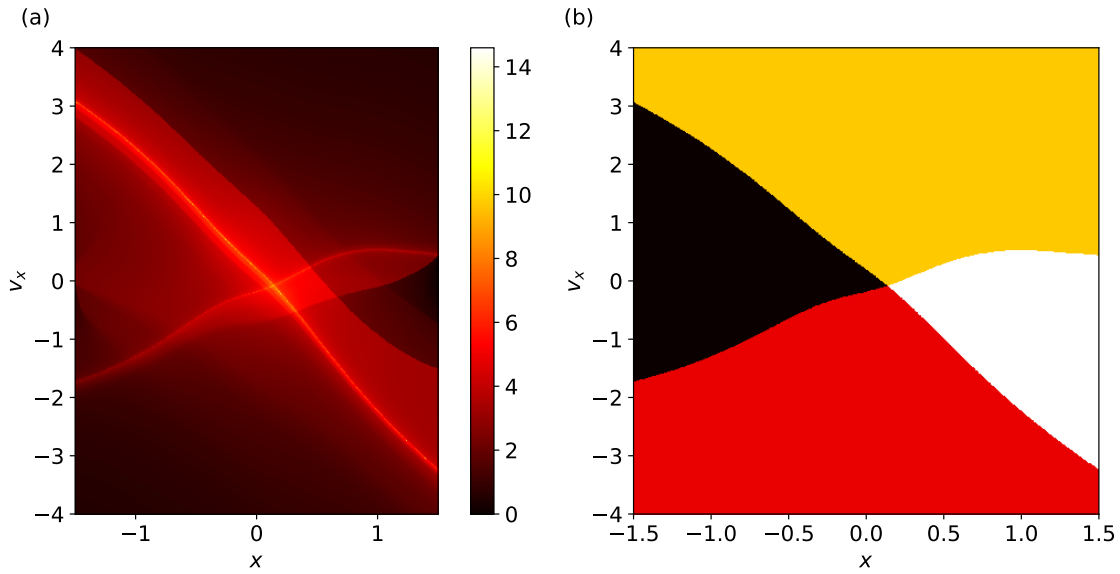

Figure 5.7.: (a): TDs of the xv_x-plane for bath coordinates $y = v_y = 0$ and time $t = 0$ for high temperature and friction. One can see the cross of the local maxima, indicating the stable and unstable manifold, as well as several crosses of plateau borders. (b): Region mapping of the same plane, showing that only the cross of the local maxima in (a) border any significant region in phase space.

borders of these trajectory regions.

5.2.3. Interpolating Noisy NHIMs

Due to the erratic nature of a NHIM's time-dependent motion, interpolating the NHIM under Langevin dynamics requires far more computational effort to produce accurate results. To train a NN that could accurately approximate the reaction coordinate for a given set of bath coordinates and time, we used approximately $120,000$ data points to train a net with three hidden layers and $(60, 140, 60)$ neurons respectively.

Using this configuration, we trained the net to approximate the NHIM of a system with high temperature and friction $k_BT = \gamma = 1$. This can be seen in Fig. 5.8. For small bath coordinates we find that the NHIM is warped in a different way than it was in the case of zero friction and noise, shown in Fig. 5.4. Interestingly, even though the NHIM's time-dependent motion is highly erratic for these parameters, its shape in phase space is similarly smooth compared to the NHIM of the noiseless system. This observation helped to determine, that the training set for the NN should be optimized for a higher resolution in time, rather than bath coordinates.

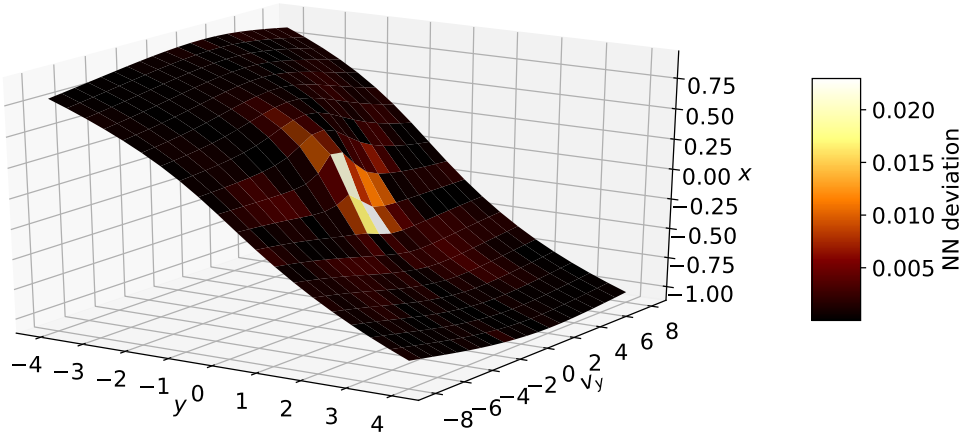

Figure 5.8.: NHIM for a system subject to Langevin dynamics for $t = 0$, $\gamma = 1$, and $k_B T = 1$. The reaction coordinate x is shown as a function of the bath coordinates y and v_y. The reaction velocity v_x has been omitted for visualization purposes. The face colors of the surface represent the deviation of the NN approximation from points computed via Binary Contraction.

5.3. Rate Calculation

Now that we have investigated the dynamics of the system thoroughly and determined how to approximate the NHIM and the DS efficiently, we can calculate the rate laws. To accomplish this, we will investigate trajectories crossing a DS constructed by projecting the reaction velocity onto the reaction coordinate.

5.3.1. Investigating the Reaction Coordinate of a Single Trajectory

A single trajectory is considered to have crossed the DS if its reaction coordinate has crossed the reaction coordinate of the NHIM associated to it. That is to say that when propagating the trajectory, the reaction coordinate of the NHIM corresponding to the bath coordinates and time of the trajectory will be approximated and compared to the reaction coordinate of the trajectory. If the reaction coordinate is lower than that of the NHIM for the same bath coordinates, then the particle will be considered a reactant. If it is larger, it will be considered a product. The reaction coordinate of a reactive trajectory and the corresponding coordinate on the NHIM can be seen in Fig. 5.9 for a system subject to Langevin dynamics. Note that although the trajectory crosses the

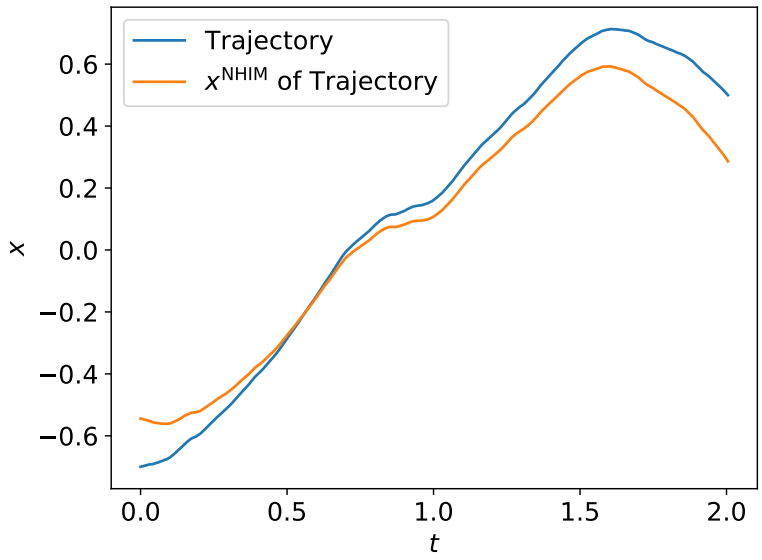

Figure 5.9.: Plot of the reaction coordinate for a single trajectory over time, together with the reaction coordinate of the NHIM for the bath coordinates of the trajectory at that time. We can see the trajectory crossing the DS at a time of roughly $t = 0.6$, transitioning from reactant to product.

NHIMs reaction coordinate for its corresponding bath coordinates, it does not cross the NHIM, as the reaction velocities differ.

5.3.2. Tracking of Crossings and Extraction of Rate Constants

By propagating a canonical ensemble from the reactant region and measuring the flux through the DS, we can determine the rate law. To do so, we tracked the crossings of every trajectory and measured the time of the first crossing. As discussed in Sec. 4.3, we extract the rate law of first order reactions from these measurements.

The time-dependent number of reactants $N_r(t)$ is shown in Fig. 5.10 for a system with temperature $k_BT = 0.4$ and friction $\gamma = 0.1$. The logarithmic plot was chosen to reveal the predominantly exponential decay over time. A settling time of the reaction can be seen in the first 1.5 time units, where the reactants $N_r(t)$ settle into an exponential decay. For long times we can see discretization errors that occur due to the discrete number of reactants. This causes function $N_r(t)$ to seem more erratic than it actually is. The problem can be dealt with by simulating a vast amount of reactants to smooth out these sudden jumps. In this particular case, a total of $2,000,000$ trajectories were computed. The high number of trajectories was necessary to obtain reliable results for the rate constants. An exponential fit of the function $N_r(t) - N_r(\text{inf}) = N_r(0)\exp(-kt)$

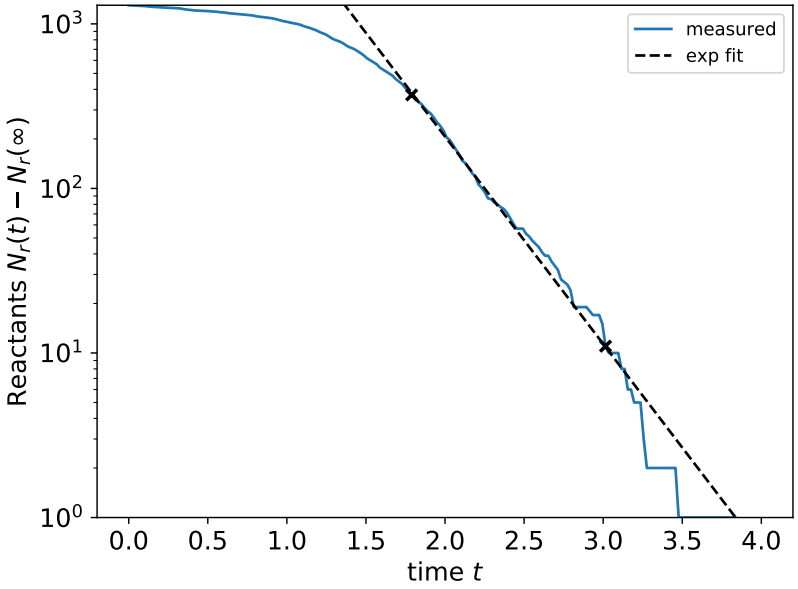

Figure 5.10.: Plot of the number of reactants over time, where the number of reactants is shown on a logarithmic scale. The dashed line indicates an exponential fit $f(t) = N_0 \exp(-kt)$, where the results are $N_0 = 68,494$ and $k = 2.901$. The crosses indicate the region where the fit was made.

was performed in the region of exponential decay, between the settling period and the region of large discretization errors. In this regime, the rate constant was determined for the first order reactions. From the fit, we find that the rate constant is $k = 2.901$. Note, that this is the result for a single stochastic force sequence and not an ensemble average of the thermalized system.

To verify that the number of recrossings is negligible, we counted the number crossings for every trajectory individually. The results are shown in Fig. 5.11, where we can see the number of recrossing trajectories compared to the number of trajectories that only cross once. In this case, the number of recrossing trajectories is negligible compared to the reactive trajectories. Considering that the approximation of the NHIM, and therefore the construction of the DS, is not exact, we can safely attribute these recrossings of the particles to numerical errors.

5.3.3. Effects of Erratic NHIM on the Rate Calculation

When friction and temperature are chosen to produce a NHIM with erratic, time-dependent motion, it is possible to find a noticeable amount of recrossings in the rate calculations. As was shown Sec. 5.2.2, the time-dependent motion of the NHIM can become highly erratic in systems with high friction and temperature.

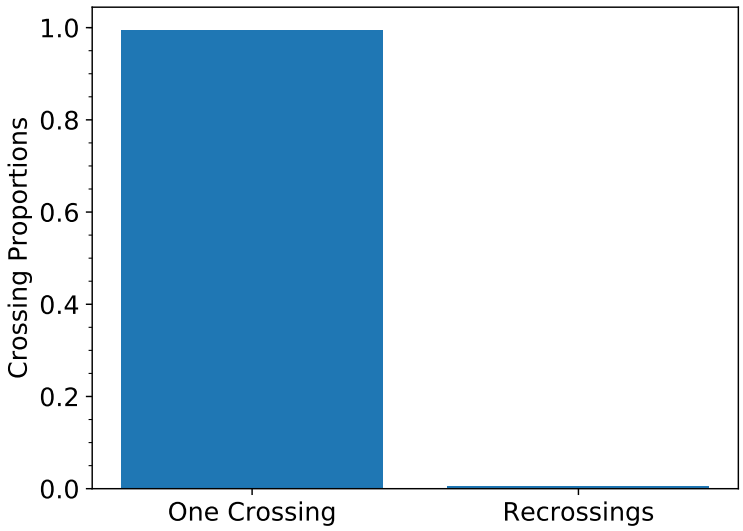

Figure 5.11.: Bar plot comparing the number of single crossings with the number of recrossing trajectories for a system with $\gamma = 0.1$ and $k_B T = 0.4$. For 1298 crossing trajectories, we have found only 7 recrossing trajectories. The bar representing the recrossings is barely discernible.

An example of such a case is shown in Fig. 5.12 (b), where we can see roughly 8% of all crossing particles are recrossing, for a system with $\gamma = 1$ and $kT = 2.0$. Consequently, the number of reactants $N_r(t)$ measured may be erroneous. In this case, even by discarding all recrossing trajectories in $N_r(t)$, we cannot observe a regime of consistent, exponential decay. Although this might imply that this is not a first order reaction, the high number of recrossings make any speculation over the rate law moot. What increases the difficulty of interpreting the rate law even further is the fact that a high friction coefficient significantly reduces the amount of particles that can cross the energy barrier. The reduction in the number of reacting particles implies that the likelihood of finding a regime of exponential decay decreases even further, as it is possible for discretization errors to become relevant during the settling time of the reaction.

As it stands, the large number of recrossings make it difficult to investigate the rate law in a high friction regime. The highly erratic motion of the NHIM prevent the NN to provide an adequate approximation. This can be seen, when comparing Figs. 5.4 and 5.8, where the approximations of the NHIM is shown for a noiseless system and a system subject to high friction and temperatures. Even when using a significantly larger NN and a much larger set of training data for the Langevin system, we can see that the errors of the approximation are roughly an order of magnitude larger compared to the noiseless system. The errors in the approximation in turn introduces large errors in the

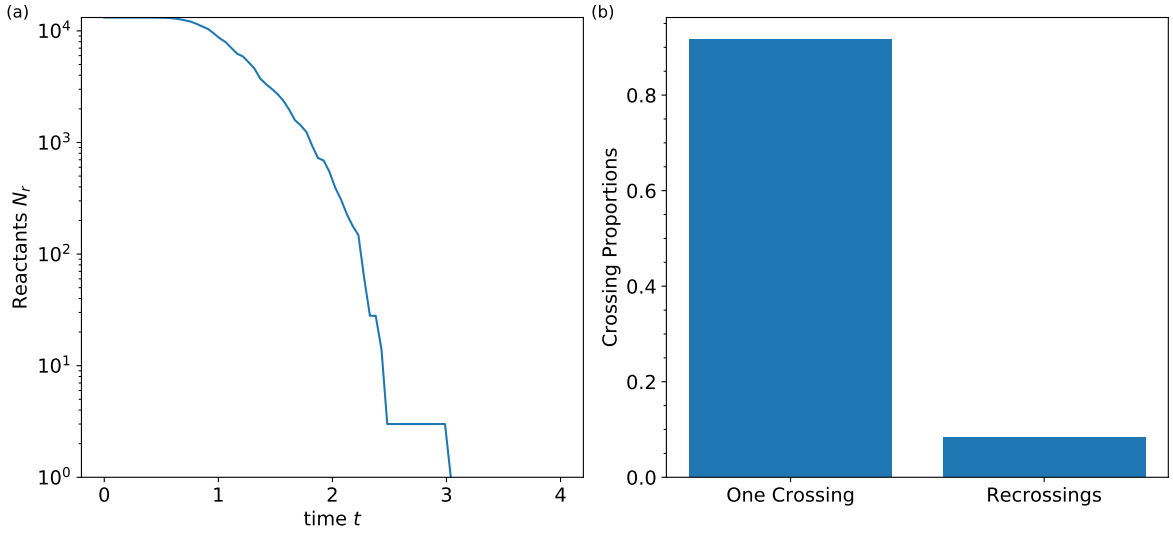

Figure 5.12.: Results of the rate calculation for a system with high friction $\gamma = 1$ and temperature $k_B T = 2$. The number of reactants over time $N_r(t)$, as seen in (a) shows, that the reactants do not reach a regime of exponential decay during the course of the reaction. Due to the high friction and temperature, a lot of recrossings are observed, as shown in (b).

time-dependent motion of the constructed DS. Due to the errors introduced to the DS used to count the crossings of trajectories, this causes recrossings in our calculations. This effect is compounded by the effect of high friction, which biases the dynamics of the system towards smaller velocities. This causes trajectories to linger in the saddle region and near the DS, which opens up opportunities to count erroneous recrossings if the DS is inaccurate.

5.3.4. Temperature Dependence of Rate Constants for Low Friction

For small friction, we can reliably obtain the rate constants of the first order reaction. To investigate the temperature dependence, we computed the rate constants for systems with friction $\gamma = 0.1$, for many temperatures. To obtain reliable results for the rate constants, we propagate ensembles of several million particles. This had the consequence, that for every set of temperature and friction, the rate constant was computed with a single noise sequence. Note, that to obtain a statistically sound result, however, the rate constants need to be averaged over several noise sequences to obtain the ensemble average.

The results for $\gamma = 0.1$ are shown in Fig. 5.13, where we obtained an activation energy of $E_a \approx 0.3482$ and a high-temperature limit for the rate constant of $A \approx 4.42$. What is evident from the fit is that the measured rate constants, especially at higher

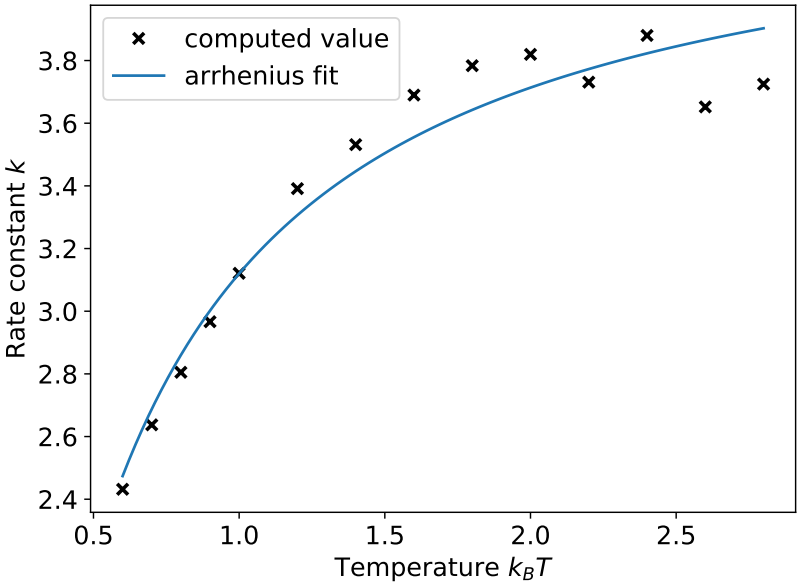

Figure 5.13.: Rate constants k computed for a system with friction $\gamma = 0.1$ over the temperature. The constants obtained here are not ensemble averages, but computed with a single, identical noise sequence. The fit of Arrhenius's equation resulted in an activation energy of $E_a \approx 0.3482$ and a high-temperature limit of $A \approx 4.42$.

temperatures, deviate in both directions around the fit. This is to be expected, as the rate constants that are computed are not ensemble averages, but rather result from a single computation. However, these results suggest that the rate constants may follow Arrhenius's law.

6. Conclusion and Outlook

In this work, we have introduced a numerical process on how to obtain rate constants for a time-dependent, rank-1 saddle potential under Langevin dynamics. An algorithm was introduced which is efficient in computing points on the time-dependent, normally hyperbolic invariant manifold of a system. These points are then used to train a neural network to provide a smooth approximation of that manifold. This in turn allowed us to construct a recrossing-free dividing surface in phase space, for which we could measure the time-dependent particle flux of reactants transitioning into products. From the time-dependent reaction rate we could then extract the rate constant of the reaction. This was done for systems subject to Langevin dynamics. It was shown that the rate constants obtained from this method follow Arrhenius's law, which provides a temperature dependent description of rate constants. Furthermore, the time-dependent motion of the invariant manifolds was investigated for different sets of friction and temperature.

When investigating the reactions of systems under high friction, we have found that the approximation with the neural network approach produces recrossings in the particle transitions. We suspect that this is due to the highly erratic, time-dependent motion of the normally hyperbolic invariant manifold, which seems to be difficult to approximate by the neural networks. This issue needs to be addressed in the future, if one aims to compute rate constants for systems with strong dissipation.

Furthermore, even though the binary contraction significantly reduces the computational time in the process of obtaining rate constants, obtaining a statistically sound rate constant would still entail the computation of several hundreds of rate constants for different noise sequences. As it stands, computing a rate constant for a single noise sequence requires roughly one CPU day of computational time. Meaning, that to obtain an adequate ensemble average over several noise sequences for a single friction and temperature combination, one needs to invest several hundreds of CPU days. Although this could be accomplished in a short amount of time by a medium-sized compute cluster, one would need to have these kinds of computational resources readily available to do so for a large set of potential parameters. The current bottle neck in the computation is the rate calculation itself, as it requires a large neural network to approximate the DS under Langevin dynamics. If one could find a way to obtain a reliable rate constant without the integration of several millions of trajectories, the computational effort could be reduced by an order of magnitude.

A. The Velocity-Verlet Integrator

Symplectic integrators are integrators that are optimized to solve Hamiltonian equations of motion. The properties of these integrators ensure, that certain properties of Hamiltonian systems are conserved. This includes properties derived from the symmetries of the system, such as energy and momentum conservation laws. Phase space geometries that are related to the dynamics of the system are also simulated accurately, such as the invariant manifolds. Due to these properties, it is important to use symplectic integrators when investigating these manifolds.

The Velocity-Verlet Integrator is a symplectic, second-order integrator that finds widespread application in most Molecular Dynamics applications. Even though it is a symplectic integrator, it can be derived from the Newtonian equation of motion, if we assume a velocity independent force F. It can be derived through the Taylor expansion of the position $x(t)$ and velocity $v(t)$

$$x(t+h) = x(t) + \dot{x}(t)h + \frac{\ddot{x}(t)}{2}h^2 + \mathcal{O}(h^3)\,, \tag{A.1}$$

$$v(t+h) = v(t) + \dot{v}(t)h + \frac{\ddot{v}(t)}{2}h^2 + \mathcal{O}(h^3)\,. \tag{A.2}$$

With the equations of motion

$$\dot{x} = v\,, \dot{v} \qquad\qquad = F(x)/m\,, \tag{A.3}$$

$$\tag{A.4}$$

where m is the inertial mass, we find

$$x(t+h) = x(t) + v(t)h + \frac{F(x(t))}{2m}h^2 + \mathcal{O}(h^3)\,, \tag{A.5}$$

$$v(t+h) = v(t) + \frac{F(x(t))}{m}h + \frac{\ddot{v}(t)}{2}h^2 + \mathcal{O}(h^3)\,. \tag{A.6}$$

All that is left to do is to find an expression for $\ddot{v}(t)$ that satisfies the order of the expansion. To this end, we perform a first-order expansion of $\dot{v}(t)$

$$\dot{v}(t+h) = \dot{v}(t) + \ddot{v}(t)h + \mathcal{O}(h^2)\,. \tag{A.7}$$

By multiplying Eq. (A.7) with h, applying the equations of motion and rearranging to solve for $\ddot{v}(t)$ we find

$$\frac{\ddot{v}(t)}{2}h^2 = \frac{h}{2m}(F(x(t+h)) - F(x(t))) + \mathcal{O}(h^3)\,. \tag{A.8}$$

Finally, by replacing the expansion parameter h with the time step Δt of the integration and substituting Eq. (A.8) into Eq. (A.6), we find

$$x(t+\Delta t) = x(t) + v(t)\Delta t + \frac{F(x(t))}{2m}(\Delta t)^2 + \mathcal{O}((\Delta t)^3)\,, \tag{A.9}$$

$$v(t+\Delta t) = v(t) + \frac{\Delta t}{2m}[F(x(t)) + F(x(t+\Delta t))] + \mathcal{O}((\Delta t)^3)\,, \tag{A.10}$$

which are the equations of the Velocity-Verlet integrator.

From the derivation it is evident that these equations provide trajectories that are accurate up to second-order terms in the time step Δt.

B. Zusammenfassung in deutscher Sprache

Diese Arbeit befasst sich mit der numerischen Anwendung der Transition State Theory zum Berechnen der Reaktionsraten von zeitabhängigen, mehrdimensionalen, Rang-1 Sattelpotentialen. Um dies zu bewerkstelligen, wird eine zeitabhängige Trennfläche im Phasenraum konstruiert, welche von jeder reaktiven Trajektorie genau einmal durchquert wird. Dies erlaubt es uns zu jedem Zeitpunkt der Reaktion die Zahl der Edukte und Produkte zu kennen.

Kapitel 2 befasst sich mit den theoretischen Grundlagen für die physikalische Modellierung chemischer Reaktionen. Hierbei werden Methoden der Molekulardynamik verwendet. Zunächst beschreiben wir, wie man aus einem quantenmechanischen System eine klassische Approximation der Dynamik erhält. Anschließend wird diskutiert, wie man mit der Methode des *minimum energy paths* Reaktionen auf statischen Potentialen beschreibt. Ein Potentialmodell wird eingeführt, mit dem typische Potentiale einer Reaktion modelliert werden können. Zusätzlich wird die Langevin Gleichung vorgestellt, welche verwendet wird um die Kopplung an ein Wärmebad zu simulieren, sowie der Einfluss von stochastischen Phänomenen.

Kapitel 3 stellt die theoretischen Grundlagen der Transition State Theorie für zeitabhängige Systeme vor. Anhand eines Beispielmodells werden hyperbolische Fixpunkte vorgestellt, sowie die invarianten Mannigfaltigkeiten der Dynamik. Eine höherdimensionale Verallgemeinerung der hyperbolischen Fixpunkte wird vorgestellt, sowie Methoden, welche benutzt werden können um invariante Mannigfaltigkeiten zu finden. Desweiteren wird diskutiert, wie man invariante Mannigfaltigkeiten dazu benutzen kann um Trennflächen zu konstruieren, welche nur einmal von reaktiven Trajektorien durchquert werden.

Kapitel 4 stellt numerische Methoden und Algorithmen vor, welche für die Untersuchung unserer Systeme verwendet werden. Es deckt die Berechnung von Punkten auf den normal hyperbolischen invarianten Mannigfaltigkeiten ab, sowie das Verwenden dieser Punkte um glatte Näherungen der gesamten Mannigfaltigkeit zu erhalten. Die binäre Kontraktionsmethode zum Erhalten dieser Punkte wird eingeführt, welche eine robuste und exponentiell schnell konvergierende Methode ist. Dieser Algorithmus basiert auf geometrischen Beobachtungen zu den invarianten Mannigfaltigkeiten im Phasenraum und benutzt Trajektorienklassifizierungen um seine Arbeit zu leisten. Wir diskutieren das Verwenden von neuronalen Netzwerken um aus den Punkten, welche mit der binären Kontraktion berechnet wurden, die Trennflächen zu approximieren, welche in Kapitel 3

vorgestellt worden.

In Kapitel 5 untersuchen wir ein Modellsystem unter Langevindynamik. Die Modelle und Methoden, welche in den vorherigen Kapiteln vorgestellt wurden, werden angewendet um die Dynamik des Systems zu untersuchen, sowie den Einfluss von Reibung und Temperatur. Die Ratengesetze wurden für verschiedene Parametersätze ausgerechnet und ausgewertet.

Es wurde gezeigt, dass die Ratenkonstanten des untersuchten Systems der Arrhenius Gleichung folgen, welche eine temperaturabhängige Beschreibung dieser Konstanten liefert. Desweiteren wurde die zeitabhängige Bewegung der Mannigfaltigkeiten in Abhängigkeit mit der Reibung und Temperatur untersucht.

Beim Untersuchen der Reaktionen in Systemen mit hoher Reibung fiel auf, dass die Näherungen der neuronalen Netzwerke dazu führen, dass einige Trajektorien mehrfach die Trennfläche durchqueren. Wir vermuten, dass die erratische, zeitabhängige Bewegung der Mannigfaltigkeiten zu den großen Fehlern in der Approximation geführt hat. Dieses Problem muss behandelt werden, falls man in Zukunft an den Ratenkonstanten von System mit hoher Dissipation interessiert ist.

Obwohl die binäre Kontraktion den Rechenaufwand für das Berechnen der Ratenkonstanten signifikant gesenkt hat, sind für das Erhalten von statistisch signifikanten Ratenkonstanten der thermalisierten System immernoch mehrere hundert Ratenrechnungen für verschiedene Rauschsequenzen notwendig. Zur Zeit benötigt eine Ratenrechnung ca. einen CPU-Tag an Rechenzeit. Dies bedeutet, dass das Berechnen einer Ratenkonstante über mehrere Rauschsequenzen hinweg hunderte von CPU-Tagen in Anspruch nehmen kann. Obwohl dies in relativ kurzer Zeit von einem mittelgroßen Rechencluster bewerkstelligt weden kann, müssen diese Rechankapazitäten frei zur Verfügung stehen um diese Rechnungen für einen großen Parametersatz durchzuführen. Zur Zeit ist das Propagieren eines Trajektorienensemble, zum Berechnen des Ratengesetzes, das größte Nadelöhr, da das neuronale Netzwerk für die Trennflächenapproximation sehr groß sein muss unter Langevindynamik. Wenn ein Weg gefunden werden könnte, mit dem man die Ratenkonstanten ohne das Integrieren von mehreren millionen Trajektorien bestimmen kann, könnte man den Rechenaufwand um eine Größenordnung vermindern.

Bibliography

[1] K. S. Pitzer, F. T. Smith, and H. Eyring. *The Transition State*. Special Publ. Chemical Society, London (1962).

[2] Philip Pechukas. Transition State Theory. *Annu. Rev. Phys. Chem.* 32, 159–177 (1981).

[3] B. C. Garrett and D. G. Truhlar. Generalized Transition State Theory. *J. Phys. Chem.* 83, 1052–1079 (1979).

[4] D. G. Truhlar, A. D. Issacson, and B. C. Garrett. *Theory of Chemical Reaction Dynamics*, volume 4, pp. 65–137. CRC Press, Boca Raton, FL (1985).

[5] Gregory A. Natanson, Bruce C. Garrett, Thanh N. Truong, Tomi Joseph, and Donald G. Truhlar. The Definition of Reaction Coordinates for Reaction-Path Dynamics. *J. Chem. Phys.* 94, 7875–7892 (1991).

[6] Donald G. Truhlar, Bruce C. Garrett, and Stephen J. Klippenstein. Current Status of Transition-State Theory. *J. Phys. Chem.* 100, 12771–12800 (1996).

[7] Donald G. Truhlar and Bruce C. Garrett. Multidimensional Transition State Theory and the Validity of Grote-Hynes Theory. *J. Phys. Chem. B* 104, 1069–1072 (2000).

[8] Tamiki Komatsuzaki and R. Stephen Berry. Dynamical hierarchy in transition states: Why and how does a system climb over the mountain? *Proc. Natl. Acad. Sci. U.S.A.* 98, 7666–7671 (2001).

[9] Holger Waalkens, Roman Schubert, and Stephen Wiggins. Wigner's dynamical transition state theory in phase space: classical and quantum. *Nonlinearity* 21, R1 (2008).

[10] Thomas Bartsch, Jeremy M. Moix, Rigoberto Hernandez, Shinnosuke Kawai, and Turgay Uzer. Time-dependent transition state theory. *Adv. Chem. Phys.* 140, 191–238 (2008).

[11] Shinnosuke Kawai and Tamiki Komatsuzaki. Robust Existence of a Reaction Boundary to Separate the Fate of a Chemical Reaction. *Phys. Rev. Lett.* 105, 048304 (2010).

[12] Rigoberto Hernandez, Thomas Bartsch, and Turgay Uzer. Transition State Theory in Liquids Beyond Planar Dividing Surfaces. *Chem. Phys.* 370, 270–276 (2010).

[13] Onise Sharia and Graeme Henkelman. Analytic dynamical corrections to transition state theory. *New J. Phys.* 18, 013023 (2016).

[14] A. J. Lichtenberg and M. A. Liebermann. *Regular and Stochastic Motion*. Springer, New York (1982).

[15] Edward Ott. *Chaos in dynamical systems*. Cambridge University Press, Cambridge, second edition edition (2002).

[16] Stephen Wiggins. *Normally hyperbolic invariant manifolds in dynamical systems*, volume 105. Springer Science & Business Media (2013).

[17] Kenichi Fukui. The path of chemical reactions - the IRC approach. *Accounts of Chemical Research* 14, 363–368 (1981).

[18] Matthias Feldmaier, Andrej Junginger, Jörg Main, Günter Wunner, and Rigoberto Hernandez. Obtaining time-dependent multi-dimensional dividing surfaces using Lagrangian descriptors. *Chem. Phys. Lett.* 687, 194 (2017).

[19] A. Einstein. Über die von der molekularkinetischen Theorie der Wärme geforderte Bewegung von in ruhenden Flüssigkeiten suspendierten Teilchen. *Annalen der Physik* 322, 549–560.

[20] A. J. Roberts. The Utility of an Invariant Manifold Description of the Evolution of a Dynamical System. *SIAM Journal on Mathematical Analysis* 20, 1447–1458 (1989).

[21] Carolina Mendoza and Ana M. Mancho. Hidden Geometry of Ocean Flows. *Phys. Rev. Lett.* 105, 038501 (2010).

[22] Ana M. Mancho, Stephen Wiggins, Jezabel Curbelo, and Carolina Mendoza. Lagrangian Descriptors: A Method for Revealing Phase Space Structures of General Time Dependent Dynamical Systems. *Commun. Nonlinear Sci. Numer. Simul.* 18, 3530 – 3557 (2013).

[23] Galen T. Craven and Rigoberto Hernandez. Lagrangian Descriptors of Thermalized Transition States on Time-Varying Energy Surfaces. *Phys. Rev. Lett.* 115, 148301 (2015).

[24] Galen T. Craven and Rigoberto Hernandez. Deconstructing field-induced ketene isomerization through Lagrangian descriptors. *Phys. Chem. Chem. Phys.* 18, 4008–4018 (2016).

[25] Matthias Feldmaier, Robin Bardakcioglu, Philippe Schraft, Johannes Reiff, Andrej Junginger, Jörg Main, Thomas Bartsch, and Rigoberto Hernandez. "Transition state theory for driven chemical reactions" in preparation.

[26] Philippe Schraft, Andrej Junginger, Matthias Feldmaier, Robin Bardakcioglu, Jörg Main, Günter Wunner, and Rigoberto Hernandez. Neural network approach to time-dependent dividing surfaces in classical reaction dynamics. *Phys. Rev. E* 97, 042309 (2018).

[27] Robin Bardakcioglu, Andrej Junginger, Matthias Feldmaier, Jörg Main, and Rigoberto Hernandez. "Binary contraction method for the construction of time-dependent dividing surfaces in driven chemical reactions" submitted.

[28] Philippe Schraft. "Neural networks for the approximation of time-dependent dividing surfaces in Transition State Theory" Master's Thesis (2017).

Acknowledgements

I thank my family and especially my parents, whose support made all of this possible.

I would also like to thank the members of the ITP1 and their attachments, for their support and wonderful discussions on all topics conceivable. Special thanks go to

- Apl. Prof. Dr. Jörg Main for his tireless efforts to provide me with opportunities to work in this field, as well as his excellent advice in a broad range of topics.
- Matthias Feldmaier, who supervised my work on this thesis as well as providing me assistance in more than just my own research. His way of viewing our work has provided me with an understanding which I could not have attained without him.
- Philippe Schraft and Robin Schuldt who worked with me during the first half of my research, and Johannes Reiff and Martin Tschöpe who worked with me during the second. They provided me with opportunities to discuss our work in a new environment.
- Holger Cartarius and Robin Gutöhrlein, who administrated the infrastructure of our institute and for providing me with assistance in my avocations at the institute.
- And especially Monika Bund, for taking care of me and the rest of the institute.

Erklärung

Ich versichere,

- dass ich diese Masterarbeit selbständig verfasst habe,
- dass ich keine anderen als die angegebenen Quellen benutzt und alle wörtlich oder sinngemäß aus anderen Werken übernommenen Aussagen als solche gekennzeichnet habe,
- dass die eingereichte Arbeit weder vollständig noch in wesentlichen Teilen Gegenstand eines anderen Prüfungsverfahrens gewesen ist,
- dass ich die Arbeit weder vollständig noch in Teilen bereits veröffentlicht habe, es sei denn, der Prüfungsausschuss hat die Veröffentlichung vorher genehmigt
- und dass das elektronische Exemplar mit den anderen Exemplaren übereinstimmt.

Stuttgart, den 25. April 2018 *Robin Bardakcioglu*